One-Dimensional/Two-Dimensional Coupling Approach with Quadrilateral Confluence Region for Modeling River Systems

Xin Liu *, Alina Chertock †, Alexander Kurganov‡, and Karlan Wolfkill§

May 24, 2019

Abstract

We study shallow water flows in river systems. An accurate description of such flows can be obtained using the two-dimensional (2-D) shallow water equations, which can be numerically solved by a shock-capturing finite-volume method. This approach can, however, be inefficient and computationally unaffordable when a large river system with many tributaries and complex geometry is to be modeled. A popular simplified approach is to model flow in each uninterrupted section of the river (called a reach) as one-dimensional (1-D) and connect the reaches at the river junctions. The flow in every reach can then be modeled using the 1-D shallow water equations, whose numerical solution is dramatically less computationally expensive compared with solving its 2-D counterpart. Even though several point-junction models are available, most of them prove to be sufficiently accurate only in the case of a smooth flow though the junction.

We propose a new 1-D/2-D river junction model, in which each reach of the river is modeled by the 1-D shallow water equations, while the confluence region, where the mixing of flows from the different directions occurs, is modeled by the 2-D ones. We define the confluence region to be a trapezoid with parallel vertical sides. This allows us to take into account both the average width of each reach and the angle between the directions of flow of the tributary and the principal river at the confluence. We choose a trapezoidal confluence region as it is consistent with the 1-D model of the river.

We implement well-balanced positivity preserving second-order semi-discrete central-upwind schemes developed in [A. Kurganov and G. Petrova, *Commun. Math. Sci.*, 5 (2007), pp. 133–160] for the 1-D shallow water equations and in [H. Shirkhani, A. Mohammadian, O. Seidou and A. Kurganov, *Comput. & Fluids*, 126 (2016), pp. 25–40] for the 2-D shallow water equations using quadrilateral grids. For the 2-D junction

*Department of Mathematics, Southern University of Science and Technology, Shenzhen, 518055, China; liux7@sustc.edu.cn

†Department of Mathematics, North Carolina State University, Raleigh, NC, 27695, USA; chertock@math.ncsu.edu

‡Department of Mathematics, Southern University of Science and Technology, Shenzhen, 518055, China and Mathematics Department, Tulane University, New Orleans, LA 70118, USA; kurganov@math.tulane.edu

§Department of Mathematics, North Carolina State University, Raleigh, NC, 27695, USA; kswolfki@ncsu.edu

simulations in the confluence region we choose a very coarse 2-D mesh as the goal of our model is not to resolve the fine details of complex 2-D vortices that form around the junction, but to efficiently compute average water depth and velocity in the connected 1-D reaches. A special ghost cell technique is developed for coupling the reaches to the confluence region, which is one of the most important parts of a good 1-D/2-D coupling method. The proposed approach leads to very significant computational savings compared to numerically solving the full 2-D problem.

We perform several numerical experiments to demonstrate plausibility of the proposed 1-D/2-D coupling model.

Key words: Shallow water flow in river systems, one-dimensional/two-dimensional coupling, quadrilateral confluence region, well-balanced central-upwind scheme.

AMS subject classification: 86A05, 86-08, 76M12, 65M08, 35L65.

1 Introduction

?⟨sec1⟩? There has been a growing interest in the scientific community in studying problems involving flows in networks formed by domains joined by junctions. In the context of shallow water applications, examples of such flows include river systems as well as man-made networks such as canals. Flow in such a network can be modeled using the two-dimensional (2-D) Saint-Venant (SV) system of shallow water equations [8]:

$$\begin{cases} h_t + (hu)_x + (hv)_y = 0 \\ (hu)_t + (hu^2 + \frac{1}{2}gh^2)_x + (huv)_y = -ghB_x, \\ (hv)_t + (huv)_x + (hv^2 + \frac{1}{2}gh^2)_y = -ghB_y, \end{cases} \tag{1.1}$$ sw2d

where $h(x,y,t)$ denotes the water depth, $u(x,y,t)$ and $v(x,y,t)$ are the x- and y-velocities, respectively, $B(x,y)$ denotes the bottom topography, and g is the gravitational constant.

2-D numerical simulations of flow in network such as river systems typically require very fine discretization in both space and time to resolve flow behavior through a junction and consequently may incur prohibitive computational costs. A common way to overcome this difficulty is to model flow in each uninterrupted section of the river (called a reach) as one-dimensional (1-D) and connect the reaches at the river junctions. For instance, in the river junction model shown in Figure 1.1, there are three reaches: the upstream reach, the downstream reach, and the tributary. Suppose, in a given reach, flow in the cross-river direction is negligible when compared to flow in the downstream direction. In this case, the system (1.1) reduces to the 1-D SV system of shallow

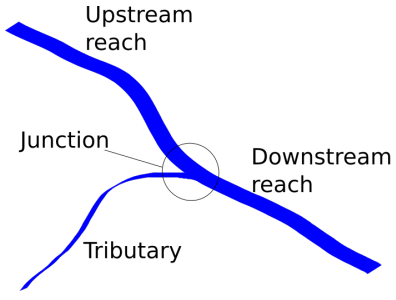

Figure 1.1: River junction.

water equations:

$$\begin{cases} h_t + (hu)_x = 0, \\ (hu)_t + (hu^2 + \frac{1}{2}gh^2)_x = -ghB_x, \end{cases} \tag{1.2}$$ sw1d

where x denotes the downstream direction for a given section of river, $h = h(x,t)$, $u = u(x,t)$ and $B = B(x)$.

We emphasize that numerically solving the 1-D system (1.2) is dramatically less computationally expensive than solving its 2-D counterpart (1.1). A key point in designing efficient numerical methods for river networks is to model the flow in each reach by the 1-D SV system and couple all of the 1-D reaches that converge to a certain junction. This should be done in a way that (i) accurately models flow through the river junction, (ii) is able to handle all flow regimes (that is, both sub-, super- and transcritical flows); (iii) captures the influence of junction geometry, and (iv) limits computational cost of numerical simulations.

Two main approaches may be identified in modeling river junctions. The first and most common approach is to model the river junction as a point; see, e.g., Figure 1.2. For subcritical flows, the connecting boundary conditions are often taken to be continuity of flow,

$$(hu)^{(R_3)}\big|_C = (hu)^{(R_1)}\big|_C + (hu)^{(R_2)}\big|_C ,$$

and continuity of either stage ($w = h + B$),

$$w^{(R_1)}\big|_C = w^{(R_2)}\big|_C = w^{(R_3)}\big|_C ,$$

or energy ($E = w + \frac{u^2}{2g}$),

$$E^{(R_1)}\big|_C = E^{(R_2)}\big|_C = E^{(R_3)}\big|_C .$$

Most of the time flow through a river junction is smooth, so a number of existing models use this condition; see, e.g., [1, 5, 7, 10, 24, 25, 30, 34, 35, 38].

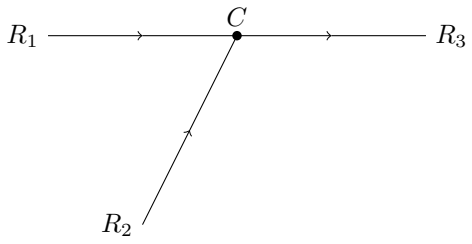

Figure 1.2: A river junction modeled as a point. R_1 and R_3 are the upstream and downstream reaches of the principal river and R_2 is the tributary. C is the point of confluence.

⟨approach1⟩

Alternatively, some models use a momentum balance at the junction point. This allows for modeling of supercritical flow and includes river width and tributary angle, [4, 28]. However, it may result in nonphysical jumps in energy for subcritical flows, [5]. For this reason, some models use a combination of energy and momentum conditions to handle sub- and supercritical flow differently; see, e.g., [5, 39].

The main advantage of modeling the junction as a point is simplicity. If the application is limited to subcritical flow, practice has shown it to work well. Some of the disadvantages are

(i) it does not work in transcritical and supercritical flow regimes; (ii) it does not capture the influence of junction geometry, when using continuity of flow and stage; (iii) there is a preferred direction of flow so that shocks traveling one direction are captured but not in another, when using momentum methods.

The second approach, taken in this paper, is to model the junctions as 2-D regions (see, e.g., Figure 1.3), solve the 2-D SV system there, and then connect the 2-D junctions to the 1-D reaches using a 1-D/2-D coupling. This approach was considered in [14, 15, 32] using a hexagonal region to represent the river junction. In [3], this approach was implemented for T-shaped regions. One advantage of the 1-D/2-D coupling approach is that the shallow water assumption is valid everywhere. This improves model consistency throughout the river junction and allows for more reliable simulations of both sub-, super- and transcritical flows.

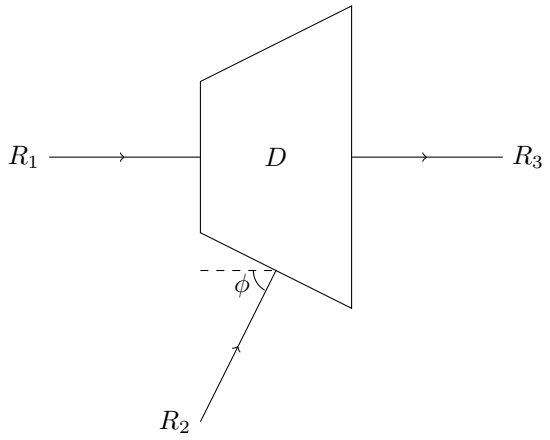

Figure 1.3: A river junction modeled as a region. R_1 and R_3 are the upstream and downstream reaches of the principal river and R_2 is the tributary. D is the confluence region.

⟨approach2a⟩

In this paper, we propose a new river junction model, in which each reach of the river is modeled by the 1-D SV system (1.2) and the confluence region, where the mixing of flows from the different directions occurs, by the 2-D SV system (1.1). We assume that x indicates the direction of flow of the main river and denote by y the direction orthogonal to x. We define the confluence region D to be a trapezoid with parallel vertical sides; see Figure 1.3. Denote the domains corresponding to upstream and downstream reaches of the principal river by R_1 and R_3, respectively, and denote by ϕ the angle between the directions of flow of the tributary R_2 and the principal river at the confluence. We choose a trapezoidal confluence region as is it consistent with the 1-D model of the river. We wish to make clear that while the trapezoidal confluence region is determined by the geometry of the actual junction, it is not a direct model of the physical river junction, but a 2-D domain on which the mixing that occurs at the junction is modeled. For this reason, a maximum angle of $\phi = \pi/2$ is sufficient in all but extreme cases. If a river junction does not fit these assumptions, a more general region D must be considered. Note that by reversing the flow, a river diversion may also be modeled using this set-up.

We implement well-balanced positivity preserving second-order semi-discrete central-upwind schemes developed in [19] for the 1-D SV system and in [33] for the 2-D SV system using quadrilateral grids. It should be observed that for the 2-D junction simulations we will choose a very coarse 2-D mesh. As the goal of this model is not to resolve the fine details of complex 2-D vortices that form around the junction, but to efficiently compute average water depth and

velocity in the connected 1-D reaches, this coarse 2-D mesh is sufficient. A special ghost cell technique will be developed for coupling the reaches to the confluence region, which is one of the most important parts of a good 1-D/2-D coupling method; see, e.g., [3, 9, 27, 31, 34, 40]. The proposed approach does not only allow one to easily model the geometry of the river junction, including relative widths of the reaches, the angle of entry of the tributary and the bottom topography, but also leads to very significant computational savings compared to solving the full 2-D problem.

The paper is organized as follows. In §2, we introduce a specific way of discretizing both the 1-D river reaches and 2-D confluence region. In §3, we describe the 1-D and 2-D second-order semi-discrete central-upwind schemes. §4 is devoted to the description of the 1-D/2-D coupling strategy. A number of numerical examples is presented in §5. Finally, in §6, we discuss possible extensions of the proposed model and directions for future work.

2 Domain Discretization

⟨sec2⟩ In this section, we introduce a specific way of discretizing both the 1-D river reaches and 2-D confluence region outlined in Figure 1.3.

2.1 Discretization of River Reaches

?⟨sec21⟩? In order to discretize a river reach as a 1-D domain, we partition the river into cells which go all the way across the river as shown in Figure 2.1. For reach R_i, $i = 1, 2, 3$, we indicate corresponding variables using superscript (R_i). We denote cell centers by $x_j^{(R_i)}$, for $j = 1, \ldots, N_i$, numbered in the direction of flow and we define additional cells, called ghost cells, extending each domain by two cells centered at $x_0^{(R_i)}$ and $x_{N_i+1}^{(R_i)}$. For the simplicity of presentation, we assume the interior cells are of uniform width $\Delta x = x_{j+\frac{1}{2}}^{(R_i)} - x_{j-\frac{1}{2}}^{(R_i)}$ within each reach R_i, but the ghost cells might be of different width. We denote these widths $\Delta x_0^{(R_i)}$ and $\Delta x_{N_i+1}^{(R_i)}$ and will explain how to determine them in §2.3 below.

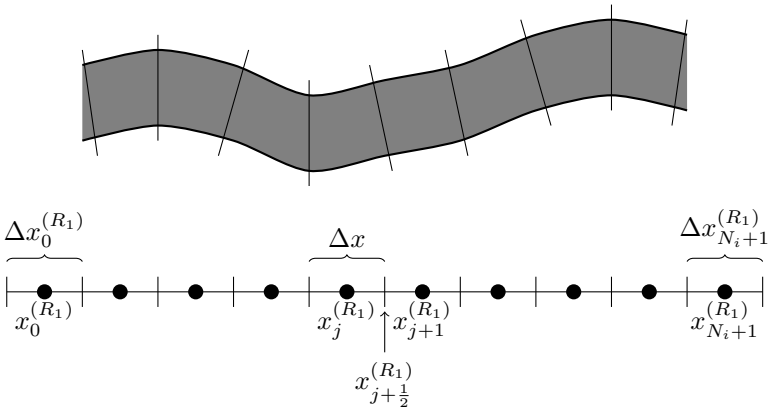

Figure 2.1: Discretization of reach R_1 as a 1-D domain. Cells centered at $x_0^{(R_1)}$ and $x_{N_1+1}^{(R_1)}$ are ghost cells.

⟨tization-1D⟩

2.2 Discretization of Confluence Region

⟨sec22⟩ Before describing the specific discretization of the trapezoidal confluence region D, we must consider the choice of dimensions of D as well as the grid size. In practice, each river junction model is intended to form a small part in a larger model representing a river system containing many reaches and junctions. As a result, computation of solution at the scale of the whole system may be dominated by computation at river junctions. It is therefore impractical to attempt to resolve 2-D waves appearing in the actual confluence region. Instead, we introduce an artificial trapezoidal domain D, designed to take into account some geometrical features of the actual confluence region and discretized using a small number of $M \times M$ cells (our numerical experiments reported in §5 indicate that $M = 4$ as in Figure 2.2 seems to be sufficient for accurate results). The size of the 2-D cells depends on the mesh size used in the 1-D reaches. Ideally, the grid size in the confluence region should be comparable to the grid size in the reaches. In this case the area of D is $\sim M^2(\Delta x)^2$, which can be smaller than the size of the actual confluence region. However, if the 1-D flow is underresolved (Δx is large), then we take the domain D to be roughly of the same size as the actual confluence region and then still split D into M^2 cells so that the grid size in D will be (much) smaller than the grid size in the reaches.

To quantify the aforementioned approach, we denote by b_i the width of reach R_i, $i = 1, 2, 3$, at the junction and distinguish between the following two cases.

Case 1. Δx is large compared to the size of the physical junction, that is, $\Delta x > \frac{1}{4}\min(b_1, b_2, b_3)$. This will likely be the case in very large river system models unless an adaptive moving mesh or adaptive mesh refinement strategy is used to enhance the resolution of strong nonsmooth waves. In this case, we define D to have side lengths b_1, b_2 and b_3 on the sides corresponding to reaches R_1, R_2 and R_3. These three side lengths together with the angle ϕ between R_1 and R_2 uniquely define the trapezoidal confluence domain D. Notice that in the case where Δx is very large, this choice of dimension may limit the size of time steps.

Case 2. Δx is small compared to the size of the physical junction. In this case, we reduce the size of the confluence region in a way that preserves the ratios of b_1, b_2 and b_3. To this end, we set the side lengths of the trapezoidal region D to be

$$b_1^* = M\Delta x b_1 \sqrt{\frac{2}{(b_1+b_3)b_2\sin\phi}}, \quad b_2^* = \frac{b_2}{b_1}\, b_1^*, \quad b_3^* = \frac{b_3}{b_1}\, b_1^*.$$

This results in a confluence region D of area $\sim (M\Delta x)^2$ with relative side lengths that reflect the geometry of the physical junction.

We now denote the centers of gravity of each 2-D cell $C_{j,k}$ by $\boldsymbol{z}_{j,k} = (x_{j,k}, y_{j,k})$ with $j, k = 1, \ldots, M$ numbered left to right and bottom to top and the cell corners by $\boldsymbol{z}_{j\pm\frac{1}{2},k\pm\frac{1}{2}}$. Note that there is no superscript, but the double subscript indicates a point in the 2-D domain.

For the three sides corresponding to reaches, we define rectangular ghost cells extending our domain in each direction as shown in Figure 2.2. These are denoted using the subscripts $j, k = 0, M+1$. Specifically, $j = 0$ corresponds to R_1, $k = 0$ corresponds to R_2, $j = M+1$ corresponds to R_3, and all having the width Δx. We set a wall boundary condition at the upper (river bank) side of D. The ghost cells on this fourth side are reflections of the interior boundary cells across the boundary; see Figure 2.2.

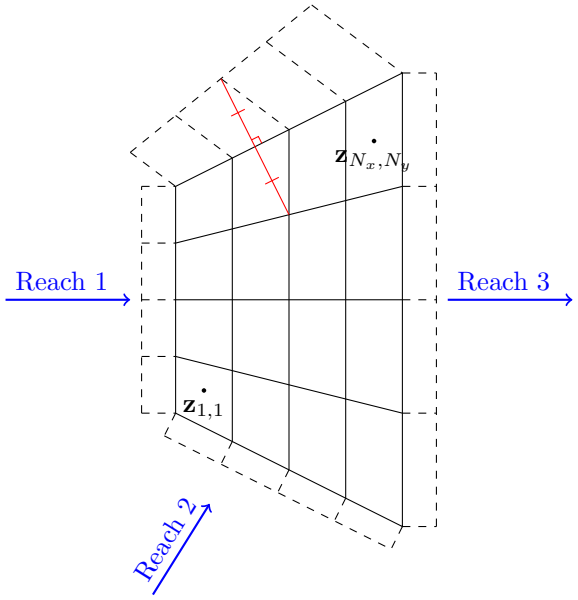

Figure 2.2: Discretization of the general confluence region D with $M = 4$. Ghost cells are shown using dotted lines. Ghost cells are rectangular on each of the sides corresponding to inflow and outflow. On the side corresponding to the river bank, ghost cells are reflections of the interior cells across the boundary.

⟨disc2d⟩

2.3 One-Dimensional Ghost Cells

⟨sec23⟩ We are now ready to give details of how to define the ghost cell widths for the 1-D reaches.

Consider the confluence region shown in Figure 2.2. Along the boundary corresponding to reach R_1, the cells are of constant width in the x-direction (the direction of R_1), so the width of the ghost cell at the right ends of R_1 is given by

$$\Delta x_{N_1+1}^{(R_1)} = x_{\frac{3}{2},k} - x_{\frac{1}{2},k}. \tag{2.1}$$ dxe1

Similarly, the width of the ghost cell at the left end of R_3 is

$$\Delta x_0^{(R_3)} = x_{M+\frac{1}{2},k} - x_{M-\frac{1}{2},k}. \tag{2.2}$$ dxw3

Note that the quantities in both (2.1) and (2.2) are independent of k.

The direction of R_2 is $(\cos\phi, \sin\phi)$, so we set the ghost cell width for the right end to be the average cell width in this direction. One way to calculate this is to set

$$\Delta x_{N_2+1}^{(R_2)} = \frac{\sin\phi}{M+1} \sum_{j=1}^{M+1} (y_{j-\frac{1}{2},\frac{3}{2}} - y_{j-\frac{1}{2},\frac{1}{2}}).$$

The other ghost cells, which are located away from the 2-D confluence region, are all set to be of width Δx, that is, $\Delta x_0^{(R_1)} = \Delta x_{N_2+1}^{(R_2)} = \Delta x_0^{(R_3)} = \Delta x$.

Equipped with the entire domain discretization, we proceed to a description of both 1-D and 2-D numerical schemes.

3 Numerical Schemes

⟨sec3⟩ The studied 1-D/2-D model of the river and tributary requires the implementation of two numerical schemes: a 1-D scheme for the river reaches and a 2-D scheme for the confluence region. In practice, any stable and sufficiently accurate schemes may be used. As an example, we use the well-balanced positivity preserving second-order semi-discrete central-upwind schemes described in [19] and [21]. In this section, we briefly describe these schemes as applied to the river junction model.

3.1 One-Dimensional Scheme

?⟨sec31⟩? In each of the river reaches R_i, $i = 1, 2, 3$, we apply the 1-D central-upwind scheme described in [19]. Since the scheme is independent of reach, we drop the reach indicator superscripts in this section.

Let us denote by $q := hu$ the discharge and introduce the vector of unknown quantities $\boldsymbol{U} := (h, q)^\top$. We also denote by

$$\overline{\boldsymbol{U}}_j(t) \approx \frac{1}{\Delta x}\int\limits_{x_{j-\frac{1}{2}}}^{x_{j+\frac{1}{2}}} \boldsymbol{U}(x,t)\,dx,$$

the cell averages of $\boldsymbol{U}$, which are assumed to be available at a certain time level t. We note that all of the computed indexed quantities will depend on t, but from now on we will omit this dependence for the sake of brevity.

Piecewise Linear Reconstruction of Equilibrium Variables. Equipped with the computed cell averages, we first approximate the solution using a global (in space) piecewise linear interpolant. Following [17, 19], we reconstruct the *equilibrium variables* $\boldsymbol{V} := (w := h + B, q)^\top$ (those that remain constant at "lake-at-rest" steady states, for which $w \equiv$ Const and $q \equiv 0$) as follows:

$$\widetilde{\boldsymbol{V}}(x) = \sum_j \boldsymbol{P}_j(x)\chi_{[x_{j-\frac{1}{2}},x_{j+\frac{1}{2}}]}(x). \tag{3.1}$$ 3.1

Here, $\chi_{[x_{j-\frac{1}{2}},x_{j+\frac{1}{2}}]}$ is the characteristic function corresponding to the jth cell and $\boldsymbol{P}_j$ is a linear function of the form

$$\boldsymbol{P}_j(x) = \overline{\boldsymbol{V}}_j + (\boldsymbol{P}_x)_j(x - x_j), \tag{3.2}$$ 3.2

where $(\boldsymbol{P}_x)_j$ are the slopes that have to be at least first-order approximations of the corresponding derivatives $\boldsymbol{V}_x(x_j, t)$. In order to make the reconstruction (3.1), (3.2) non-oscillatory, the slopes $(\boldsymbol{P}_x)_j$ are to be computed using a nonlinear limiter. A library of such limiters is available; see, e.g., [11, 16, 23] and references therein. In the numerical experiments reported in §5, we have used the generalized minmod limiter (see, e.g., [29, 36, 37]):

$$(\boldsymbol{P}_x)_j = \text{minmod}\left(\kappa\,\frac{\overline{\boldsymbol{V}}_{j+1} - \overline{\boldsymbol{V}}_j}{\Delta x},\ \frac{\overline{\boldsymbol{V}}_{j+1} - \overline{\boldsymbol{V}}_{j-1}}{2\Delta x},\ \kappa\,\frac{\overline{\boldsymbol{V}}_j - \overline{\boldsymbol{V}}_{j-1}}{\Delta x}\right) \tag{3.3}$$ 3.2a

applied in a componentwise manner. Here, $\overline{\boldsymbol{V}}_j = (\overline{w}_j, \bar{q}_j)^\top$, $\overline{w}_j := \overline{h}_j + \overline{B}_j$, where the quantity $\overline{B}_j$ is defined below, $\kappa \in [1,2]$ is a parameter that controls the amount of numerical diffusion in the overall method—larger values of κ correspond to sharper reconstructions, but typically lead to (slightly) more oscillatory results, and the minmod function is defined by

$$\operatorname{minmod}(a_1, a_2, \ldots) = \begin{cases} \min(a_1, a_2, \ldots), & \text{if } a_i > 0, \forall i \\ \max(a_1, a_2, \ldots), & \text{if } a_i < 0, \forall i \\ 0, & \text{otherwise.} \end{cases}$$

After reconstructing $\widetilde{\boldsymbol{V}}$, we compute the left and right point values of $\boldsymbol{V}$ at each cell interface:

$$\boldsymbol{V}^-_{j+\frac{1}{2}} = \boldsymbol{P}_j(x_{j+\frac{1}{2}}) \quad \text{and} \quad \boldsymbol{V}^+_{j+\frac{1}{2}} = \boldsymbol{P}_{j+1}(x_{j+\frac{1}{2}}), \tag{3.4}$$ 3.2b

and then obtain the one-sided point values of the water depth $h^\pm_{j+\frac{1}{2}} = w^\pm_{j+\frac{1}{2}} - B_{j+\frac{1}{2}}$, where $B_{j+\frac{1}{2}} = B(x_{j+\frac{1}{2}})$ if B is continuous and $B_{j+\frac{1}{2}} = \frac{1}{2}\big[\lim_{x\to x^+_{j+\frac{1}{2}}} B(x) + \lim_{x\to x^-_{j+\frac{1}{2}}} B(x)\big]$ otherwise.

Continuous Piecewise Linear Approximation of the Bottom Topography. Following [19], we replace the given bottom topography function B with its continuous piecewise linear approximant

$$\widetilde{B}(x) = B_{j-\frac{1}{2}} + \big(B_{j+\frac{1}{2}} - B_{j-\frac{1}{2}}\big) \cdot \frac{x - x_{j-\frac{1}{2}}}{\Delta x}, \quad x_{j-\frac{1}{2}} \le x \le x_{j+\frac{1}{2}}.$$

This choice of approximation has several advantages. First, the cell center values for $\widetilde{B}$,

$$B_j := \frac{B_{j+\frac{1}{2}} + B_{j-\frac{1}{2}}}{2} = \overline{B}_j,$$

are equal to the cell averages of $\widetilde{B}$. Also, the approximation is second order accurate so that the overall accuracy of the method is unchanged. Furthermore, this approximation will allow one to easily enforce the positivity of the reconstructed water depth after the following positivity correction procedure is implemented.

Positivity Preserving Correction of $\widetilde{w}$. We note that the use of aforementioned nonlinear limiters cannot prevent appearance of negative point values of $h^-_{j+\frac{1}{2}}$ or $h^+_{j-\frac{1}{2}}$ at the cell interfaces in cells where $\overline{h}_j$ is very close to B_j. Following [19], we correct the reconstruction of $\widetilde{w}$ in the following conservative way:

1. If $w^-_{j+\frac{1}{2}} < B_{j+\frac{1}{2}}$, then set $w^-_{j+\frac{1}{2}} = B_{j+\frac{1}{2}}$ and $w^+_{j-\frac{1}{2}} = 2\overline{w}_j - B_{j+\frac{1}{2}}$, and consequently $h^-_{j+\frac{1}{2}} = 0$ and $h^+_{j-\frac{1}{2}} = 2\,(\overline{w}_j - \overline{B}_j)$.
2. If $w^+_{j-\frac{1}{2}} < B_{j-\frac{1}{2}}$, then set $w^+_{j-\frac{1}{2}} = B_{j-\frac{1}{2}}$ and $w^-_{j+\frac{1}{2}} = 2\overline{w}_j - B_{j-\frac{1}{2}}$, and consequently $h^+_{j-\frac{1}{2}} = 0$ and $h^-_{j-\frac{1}{2}} = 2\,(\overline{w}_j - \overline{B}_j)$.

Time Evolution. We use the semi-discrete central-upwind scheme from [19] and evolve the cell averages of $\boldsymbol{U}$ in time by solving the following system of ODEs:

$$\frac{d}{dt}\overline{\boldsymbol{U}}_j = -\frac{\boldsymbol{H}_{j+\frac12}-\boldsymbol{H}_{j-\frac12}}{\Delta x}+\overline{\boldsymbol{S}}_j, \tag{3.5}$$ sd1d

where

$$H_{j+\frac12}=\frac{a^+_{j+\frac12}\boldsymbol{F}\big(\boldsymbol{U}^-_{j+\frac12}\big)-a^-_{j+\frac12}\boldsymbol{F}\big(\boldsymbol{U}^+_{j+\frac12}\big)}{a^+_{j+\frac12}-a^-_{j+\frac12}}+\frac{a^+_{j+\frac12}a^-_{j+\frac12}}{a^+_{j+\frac12}-a^-_{j+\frac12}}\Big[\boldsymbol{U}^+_{j+\frac12}-\boldsymbol{U}^-_{j+\frac12}\Big] \tag{3.6}$$ nf

are central-upwind numerical fluxes and $\boldsymbol{F}(\boldsymbol{U})=\big(q,\frac{q^2}{h}+\frac12 gh^2\big)^\top$ denote the flux.

In (3.5), the source term $\overline{\boldsymbol{S}}_j$ is computed in a well-balanced manner (see [17, 19]):

$$\overline{\boldsymbol{S}}_j=\left(0,-g\overline{h}_j\,\frac{B_{j+\frac12}-B_{j-\frac12}}{\Delta x}\right)^\top.$$

In (3.6), $a^\pm_{j+\frac12}$ are one-sided local speeds of propagation determined by the eigenvalues of the flux Jacobian $\frac{\partial \boldsymbol{F}}{\partial \boldsymbol{U}}$; see [18]. For the SV system (1.2), the eigenvalues of the Jacobian are $u\pm\sqrt{gh}$, and therefore

$$\begin{aligned}
a^-_{j+\frac12}&=\min\left\{u^-_{j+\frac12}-\sqrt{gh^-_{j+\frac12}},\,u^+_{j+\frac12}-\sqrt{gh^+_{j+\frac12}},\,0\right\},\\
a^+_{j+\frac12}&=\max\left\{u^-_{j+\frac12}+\sqrt{gh^-_{j+\frac12}},\,u^+_{j+\frac12}+\sqrt{gh^+_{j+\frac12}},\,0\right\}.
\end{aligned}$$

We finally note that in order to evaluate the one-sided local speeds of propagation and numerical fluxes one needs to compute the point values of the velocity $u^\pm_{j+\frac12}$. In principle, $u=q/h$, but this formula should be desingularized to avoid division by zero or by very small values of h. This can be done in many different ways, for example, by setting

$$u^\pm_{j+\frac12}=\frac{\sqrt{2}\,h^\pm_{j+\frac12}q^\pm_{j+\frac12}}{\sqrt{(h^\pm_{j+\frac12})^4+\max\big\{(h^\pm_{j+\frac12})^4,\varepsilon\big\}}}, \tag{3.7}$$ 3.5

where ε is a very small number; see [19] for discussion on different desingularization strategies. For consistency, after computing $u^\pm_{j+\frac12}$ using (3.7) we need to recompute $q^\pm_{j+\frac12}=h^\pm_{j+\frac12}\cdot u^\pm_{j+\frac12}$.

3.2 Two-Dimensional Numerical Scheme

⟨sec32⟩ For the confluence region described in §2.2, we use the well-balanced and positivity preserving method for structured quadrilateral grids described in [21]; see also [20] for the derivation of the central-upwind fluxes on quadrilateral grids and [33] for the central-upwind scheme for unstructured quadrilateral grids.

Let us denote the 2-D velocity vector by $\boldsymbol{u}:=(u,v)^\top$ and the discharge vector by $\boldsymbol{q}:=h\boldsymbol{u}=(hu,hv)^\top$. The vector of unknowns in the confluence region is then denoted by $\boldsymbol{\mathcal{U}}:=(h,\boldsymbol{q})^\top$ and its cell averages over cell $C_{j,k}$ by

$$\overline{\boldsymbol{\mathcal{U}}}_{j,k}(t)=\frac{1}{|C_{j,k}|}\int\limits_{C_{j,k}}\boldsymbol{\mathcal{U}}(\boldsymbol{z},t)\,d\boldsymbol{z},\quad \boldsymbol{z}:=(x,y).$$

As in the previous section, we will omit writing the dependence on t.

Piecewise Linear Reconstruction of Equilibrium Variables. As in the 1-D case, we approximate the solution using a piecewise linear interpolant by reconstructing equilibrium variables $\boldsymbol{\mathcal{V}} := (w := h + B, \boldsymbol{q})^\top$. We denote this approximation by

$$\widetilde{\boldsymbol{\mathcal{V}}}(\boldsymbol{z}) = \sum_{j,k} \boldsymbol{\mathcal{P}}_{j,k}(\boldsymbol{z}) \chi_{C_{j,k}},$$

where $\chi_{C_{j,k}}$ is the characteristic function corresponding to cell $C_{j,k}$ and $\boldsymbol{\mathcal{P}}_{j,k}(\boldsymbol{z})$ is a linear function of the form

$$\boldsymbol{\mathcal{P}}_{j,k}(\boldsymbol{z}) = \overline{\boldsymbol{\mathcal{V}}}_{j,k} + (\boldsymbol{\mathcal{P}}_{j,k})_x (x - x_j) + (\boldsymbol{\mathcal{P}}_{j,k})_y (y - y_k).$$

Here, $\overline{\boldsymbol{\mathcal{V}}}_{j,k} = (\overline{w}_{j,k}, \overline{\boldsymbol{q}}_{j,k})^\top$, $\overline{w}_{j,k} = \overline{h}_{j,k} + B_{j,k}$, where $B_{j,k}$ is defined below, and $(\boldsymbol{\mathcal{P}}_{j,k})_x$ and $(\boldsymbol{\mathcal{P}}_{j,k})_y$ are approximations of $\boldsymbol{\mathcal{V}}_x(\boldsymbol{z}_{j,k})$ and $\boldsymbol{\mathcal{V}}_y(\boldsymbol{z}_{j,k})$, respectively. Since the computational cells are non-rectangular, estimating these derivatives is nontrivial. There are several ways to do this. We estimate them in a two-step process following [33]. First, for each cell, we construct four linear interpolants on the triangles shown in Figure 3.1 and compute the x- and y-derivatives of these interpolants. Next, we use these derivatives together with a minmod slope limiter to estimate the slopes for each cell in a way that avoids numerical oscillations and preserves cell averages.

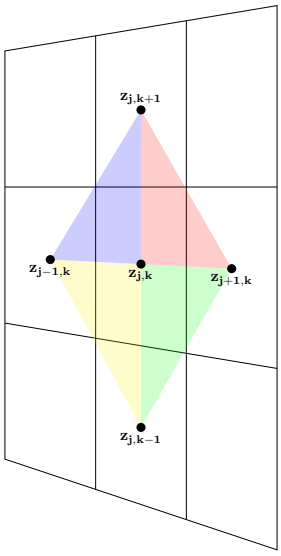

Figure 3.1: Linear reconstruction for 2-D structured grid.

For the first step, let $(\boldsymbol{\mathcal{V}}_{j,k})_x^{+,+}$ and $(\boldsymbol{\mathcal{V}}_{j,k})_y^{+,+}$ denote the x- and y-derivatives of the component-wise linear interpolant $\widetilde{\boldsymbol{\mathcal{V}}}$ through the points $\boldsymbol{z}_{j,k}$, $\boldsymbol{z}_{j+1,k}$ and $\boldsymbol{z}_{j,k+1}$. Similarly, let $(\boldsymbol{\mathcal{V}}_{j,k})_x^{+,-}$ and $(\boldsymbol{\mathcal{V}}_{j,k})_y^{+,-}$ denote the x- and y-derivatives of the interpolant through the points $\boldsymbol{z}_{j,k}$, $\boldsymbol{z}_{j+1,k}$ and $\boldsymbol{z}_{j,k-1}$; let $(\boldsymbol{\mathcal{V}}_{j,k})_x^{-,-}$ and $(\boldsymbol{\mathcal{V}}_{j,k})_y^{-,-}$ denote the x- and y-derivatives of the interpolant through the points $\boldsymbol{z}_{j,k}$, $\boldsymbol{z}_{j-1,k}$ and $\boldsymbol{z}_{j,k-1}$; and let $(\boldsymbol{\mathcal{V}}_{j,k})_x^{-,+}$ and $(\boldsymbol{\mathcal{V}}_{j,k})_y^{-,+}$ denote the x- and y-derivatives interpolant through the points $\boldsymbol{z}_{j,k}$, $\boldsymbol{z}_{j-1,k}$ and $\boldsymbol{z}_{j,k+1}$.

We now set

$$(\boldsymbol{\mathcal{P}}_{j,k})_x = \text{minmod}\Big(\kappa\,(\boldsymbol{\mathcal{V}}_{j,k})_x^{+,+}, \kappa\,(\boldsymbol{\mathcal{V}}_{j,k})_x^{+,-}, \kappa\,(\boldsymbol{\mathcal{V}}_{j,k})_x^{-,-}, \kappa\,(\boldsymbol{\mathcal{V}}_{j,k})_x^{-,+}, \frac{1}{4}\left[(\boldsymbol{\mathcal{V}}_{j,k})_x^{+,+} + (\boldsymbol{\mathcal{V}}_{j,k})_x^{+,-} + (\boldsymbol{\mathcal{V}}_{j,k})_x^{-,-} + (\boldsymbol{\mathcal{V}}_{j,k})_x^{-,+}\right]\Big)$$

and

$$(\boldsymbol{\mathcal{P}}_{j,k})_y = \text{minmod}\Big(\kappa\,(\boldsymbol{\mathcal{V}}_{j,k})_y^{+,+}, \kappa\,(\boldsymbol{\mathcal{V}}_{j,k})_y^{+,-}, \kappa\,(\boldsymbol{\mathcal{V}}_{j,k})_y^{-,-}, \kappa\,(\boldsymbol{\mathcal{V}}_{j,k})_y^{-,+}, \frac{1}{4}\left[(\boldsymbol{\mathcal{V}}_{j,k})_y^{+,+} + (\boldsymbol{\mathcal{V}}_{j,k})_y^{+,-} + (\boldsymbol{\mathcal{V}}_{j,k})_y^{-,-} + (\boldsymbol{\mathcal{V}}_{j,k})_y^{-,+}\right]\Big),$$

where $1 \le \kappa \le 2$ is a minmod parameter with higher values giving sharper but possibly more oscillatory solutions.

Lastly, we define approximate cell edge values

$$\boldsymbol{\mathcal{V}}_{j,k}^{\mathrm{E}} := \boldsymbol{\mathcal{P}}_{j,k}(\boldsymbol{z}_{j+1,k}), \quad \boldsymbol{\mathcal{V}}_{j,k}^{\mathrm{W}} := \boldsymbol{\mathcal{P}}_{j,k}(\boldsymbol{z}_{j-1,k}), \quad \boldsymbol{\mathcal{V}}_{j,k}^{\mathrm{N}} := \boldsymbol{\mathcal{P}}_{j,k}(\boldsymbol{z}_{j,k+1}), \quad \boldsymbol{\mathcal{V}}_{j,k}^{\mathrm{S}} := \boldsymbol{\mathcal{P}}_{j,k}(\boldsymbol{z}_{j,k-1}),$$

where $\boldsymbol{z}_{j\pm\frac12,k}$ and $\boldsymbol{z}_{j,k\pm\frac12}$ are cell edge midpoints as shown in Figure 3.2.

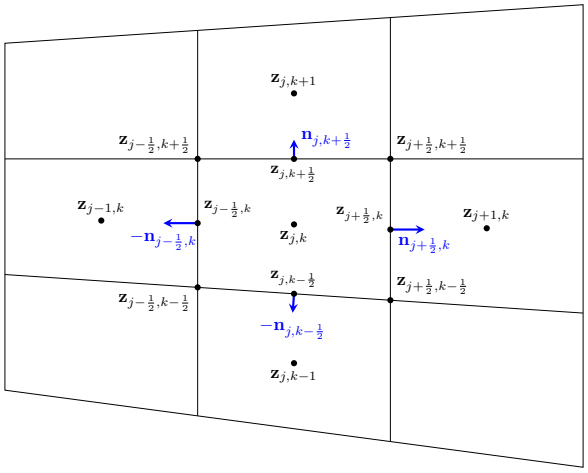

Figure 3.2: Notation for 2-D grid.

Continuous Piecewise Linear Approximation of the Bottom Topography. As in the 1-D case, we approximate the bottom topography with a continuous piecewise linear approximation. We follow the method proposed in [33], according to which the bottom interpolant $\widetilde{B}(\boldsymbol{z})$ in each quadrilateral cell $C_{j,k}$ consists of four continuously connected linear pieces constructed over the following four triangles shown in Figure 3.3: $T_{j,k}^{\mathrm{W}}$ (the triangle with vertices $\boldsymbol{z}_{j,k}$, $\boldsymbol{z}_{j-\frac12,k-\frac12}$ and $\boldsymbol{z}_{j-\frac12,k+\frac12}$), $T_{j,k}^{\mathrm{E}}$ (the triangle with vertices $\boldsymbol{z}_{j,k}$, $\boldsymbol{z}_{j+\frac12,k-\frac12}$ and $\boldsymbol{z}_{j+\frac12,k+\frac12}$), $T_{j,k}^{\mathrm{S}}$ (the triangle with vertices $\boldsymbol{z}_{j,k}$, $\boldsymbol{z}_{j-\frac12,k-\frac12}$ and $\boldsymbol{z}_{j+\frac12,k-\frac12}$) and $T_{j,k}^{\mathrm{N}}$ (the triangle with vertices $\boldsymbol{z}_{j,k}$, $\boldsymbol{z}_{j-\frac12,k+\frac12}$ and $\boldsymbol{z}_{j+\frac12,k+\frac12}$).

In order to complete the construction of $\widetilde{B}$, we need to specify the point values of $\widetilde{B}$ at each of the aforementioned triangle vertices: $\boldsymbol{z}_{j,k}$, $\boldsymbol{z}_{j-\frac12,k-\frac12}$, $\boldsymbol{z}_{j+\frac12,k-\frac12}$, $\boldsymbol{z}_{j-\frac12,k+\frac12}$ and $\boldsymbol{z}_{j+\frac12,k+\frac12}$. This can be done as follows. First, we set the values of $\widetilde{B}$ at the corners of $C_{j,k}$:

$$B_{j\pm\frac12,k\pm\frac12} := \widetilde{B}\big(\boldsymbol{z}_{j\pm\frac12,k\pm\frac12}\big) = B\big(\boldsymbol{z}_{j\pm\frac12,k\pm\frac12}\big) \quad \text{and} \quad B_{j\pm\frac12,k\mp\frac12} := \widetilde{B}\big(\boldsymbol{z}_{j\pm\frac12,k\mp\frac12}\big) = B\big(\boldsymbol{z}_{j\pm\frac12,k\mp\frac12}\big).$$

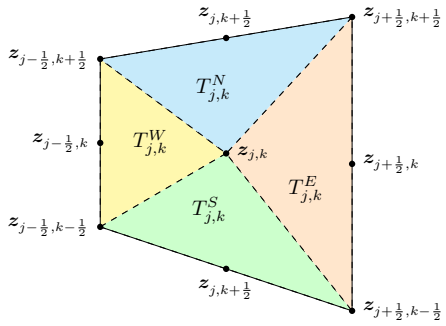

Figure 3.3: Cell $C_{i,j}$ with sub-triangles used in the linear approximation of the bottom topography.
subtriangles⟩

Second, we obtain the values of $\widetilde{B}$ at the cell edge centers:

$$B_{j\pm\frac{1}{2},k} := \widetilde{B}\big(\boldsymbol{z}_{j\pm\frac{1}{2},k}\big) = \frac{B\big(\boldsymbol{z}_{j\pm\frac{1}{2},k+\frac{1}{2}}\big) + B\big(\boldsymbol{z}_{j\pm\frac{1}{2},k-\frac{1}{2}}\big)}{2},$$
$$B_{j,k\pm\frac{1}{2}} := \widetilde{B}\big(\boldsymbol{z}_{j,k\pm\frac{1}{2}}\big) = \frac{B\big(\boldsymbol{z}_{j+\frac{1}{2},k\pm\frac{1}{2}}\big) + B\big(\boldsymbol{z}_{j-\frac{1}{2},k\pm\frac{1}{2}}\big)}{2},$$

which are then averaged with appropriate weights to give the following cell center value:

$$B_{j,k} := \widetilde{B}(\boldsymbol{z}_{j,k}) = \frac{1}{|C_{j,k}|}\left(\left|T^{\mathrm{W}}_{j,k}\right| B_{j-\frac{1}{2},k} + \left|T^{\mathrm{E}}_{j,k}\right| B_{j+\frac{1}{2},k} + \left|T^{\mathrm{S}}_{j,k}\right| B_{j,k-\frac{1}{2}} + \left|T^{\mathrm{N}}_{j,k}\right| B_{j,k+\frac{1}{2}}\right).$$

Positivity Preserving Correction. At this point, we can recover cell edge center values for the water depth $h^{\mathrm{E}}_{j,k} = w^{\mathrm{E}}_{j,k} - B_{j+\frac{1}{2},k}$, $h^{\mathrm{W}}_{j,k} = w^{\mathrm{W}}_{j,k} - B_{j-\frac{1}{2},k}$, $h^{\mathrm{N}}_{j,k} = w^{\mathrm{N}}_{j,k} - B_{j,k+\frac{1}{2}}$ and $h^{\mathrm{S}}_{j,k} = w^{\mathrm{S}}_{j,k} - B_{j,k-\frac{1}{2}}$. This reconstruction, however, does not guarantee that h will remain non-negative; so following [17] we reconstruct h instead of w in dry or near dry cells. We consider a cell to be near dry if

$$\min\left\{\overline{w}_{j,k}, \overline{w}_{j\pm1,k}, \overline{w}_{j,k\pm1}\right\} < \max\left\{B_{j,k}, B_{j\pm1,k}, B_{j,k\pm1}\right\}$$

or $\overline{h}_{j,k} = \overline{w}_{j,k} - B_{j,k} < \tau$ for some tolerance $0 < \tau << 1$.

Time Evolution. We evolve the cell averages of $\boldsymbol{\mathcal{U}}$ using the semi-discrete central-upwind scheme:

$$\frac{d}{dt}\overline{\boldsymbol{\mathcal{U}}}_{j,k}(t) = -\frac{1}{|C_{j,k}|}\left(\boldsymbol{\mathcal{H}}_{j+\frac{1}{2},k} - \boldsymbol{\mathcal{H}}_{j-\frac{1}{2},k} + \boldsymbol{\mathcal{H}}_{j,k+\frac{1}{2}} - \boldsymbol{\mathcal{H}}_{j,k-\frac{1}{2}}\right) + \boldsymbol{\mathcal{S}}_{j,k}, \tag{3.8}$$ sd2d

where the numerical fluxes are defined by

$$\begin{aligned}\boldsymbol{\mathcal{H}}_{j+\frac12,k}=\frac{\ell_{j+\frac12,k}}{a^+_{j+\frac12,k}-a^-_{j+\frac12,k}}\Big(&\cos\left(\theta_{j+\frac12,k}\right)\left[a^+_{j+\frac12,k}\boldsymbol{\mathcal{F}}\left(\boldsymbol{\mathcal{U}}^{\rm E}_{j,k}\right)-a^-_{j+\frac12,k}\boldsymbol{\mathcal{F}}\left(\boldsymbol{\mathcal{U}}^{\rm W}_{j+1,k}\right)\right]\\&+\sin\left(\theta_{j+\frac12,k}\right)\left[a^+_{j+\frac12,k}\boldsymbol{\mathcal{G}}\left(\boldsymbol{\mathcal{U}}^{\rm E}_{j,k}\right)-a^-_{j+\frac12,k}\boldsymbol{\mathcal{G}}\left(\boldsymbol{\mathcal{U}}^{\rm W}_{j+1,k}\right)\right]\\&+a^+_{j+\frac12,k}a^-_{j+\frac12,k}\left(\boldsymbol{\mathcal{U}}^{\rm W}_{j+1,k}-\boldsymbol{\mathcal{U}}^{\rm E}_{j,k}\right)\Big),\\
\boldsymbol{\mathcal{H}}_{j,k+\frac12}=\frac{\ell_{j,k+\frac12}}{b^+_{j,k+\frac12}-b^-_{j,k+\frac12}}\Big(&\cos\left(\theta_{j,k+\frac12}\right)\left[b^+_{j,k+\frac12}\boldsymbol{\mathcal{F}}\left(\boldsymbol{\mathcal{U}}^{\rm N}_{j,k}\right)-b^-_{j,k+\frac12}\boldsymbol{\mathcal{F}}\left(\boldsymbol{\mathcal{U}}^{\rm S}_{j,k+1}\right)\right]\\&+\sin\left(\theta_{j,k+\frac12}\right)\left[b^+_{j,k+\frac12}\boldsymbol{\mathcal{G}}\left(\boldsymbol{\mathcal{U}}^{\rm N}_{j,k}\right)-b^-_{j,k+\frac12}\boldsymbol{\mathcal{G}}\left(\boldsymbol{\mathcal{U}}^{\rm S}_{j,k+1}\right)\right]\\&+b^+_{j,k+\frac12}b^-_{j,k+\frac12}\left(\boldsymbol{\mathcal{U}}^{\rm S}_{j+1,k}-\boldsymbol{\mathcal{U}}^{\rm N}_{j,k}\right)\Big).\end{aligned}$$

Here, $\boldsymbol{\mathcal{F}}(\boldsymbol{\mathcal{U}})=\left(hu,hu^2+\frac12gh^2,huv\right)^\top$ and $\boldsymbol{\mathcal{G}}(\boldsymbol{\mathcal{U}})=\left(hv,huv,hv^2+\frac12gh^2\right)^\top$ are the shallow water fluxes; $\ell_{j+\frac12,k}:=|\boldsymbol{z}_{j+\frac12,k+\frac12}-\boldsymbol{z}_{j+\frac12,k-\frac12}|$ and $\ell_{j,k+\frac12}:=|\boldsymbol{z}_{j+\frac12,k+\frac12}-\boldsymbol{z}_{j-\frac12,k+\frac12}|$ are cell edge lengths and $\boldsymbol{n}_{j+\frac12,k}=\left(\cos(\theta_{j+\frac12,k}),\sin(\theta_{j+\frac12,k})\right)^\top$ and $\boldsymbol{n}_{j,k+\frac12}=\left(\cos(\theta_{j,k+\frac12}),\sin(\theta_{j,k+\frac12})\right)^\top$ are unit outward normal vectors as shown in Figure 3.2.

The one-sided local speeds of propagation, $a^\pm$ and $b^\pm$, are estimated by the maximum positive and minimum negative eigenvalues of the Jacobian of the corresponding directional flux:

$$\begin{aligned}a^+_{j+\frac12,k}&=\max\left\{\boldsymbol{u}^{\rm E}_{j,k}\cdot\boldsymbol{n}_{j+\frac12,k}+\sqrt{gh^{\rm E}_{j,k}},\ \boldsymbol{u}^{\rm W}_{j+1,k}\cdot\boldsymbol{n}_{j+\frac12,k}+\sqrt{gh^{\rm W}_{j+1,k}},\ 0\right\},\\
a^-_{j+\frac12,k}&=\min\left\{\boldsymbol{u}^{\rm E}_{j,k}\cdot\boldsymbol{n}_{j+\frac12,k}-\sqrt{gh^{\rm E}_{j,k}},\ \boldsymbol{u}^{\rm W}_{j+1,k}\cdot\boldsymbol{n}_{j+\frac12,k}-\sqrt{gh^{\rm W}_{j+1,k}},\ 0\right\},\\
b^+_{j,k+\frac12}&=\max\left\{\boldsymbol{u}^{\rm N}_{j,k}\cdot\boldsymbol{n}_{j,k+\frac12}+\sqrt{gh^{\rm N}_{j,k}},\ \boldsymbol{u}^{\rm S}_{j,k+1}\cdot\boldsymbol{n}_{j,k+\frac12}+\sqrt{gh^{\rm S}_{j,k+1}},\ 0\right\},\\
b^-_{j,k+\frac12}&=\min\left\{\boldsymbol{u}^{\rm N}_{j,k}\cdot\boldsymbol{n}_{j,k+\frac12}-\sqrt{gh^{\rm N}_{j,k}},\ \boldsymbol{u}^{\rm S}_{j,k+1}\cdot\boldsymbol{n}_{j,k+\frac12}-\sqrt{gh^{\rm S}_{j,k+1}},\ 0\right\}.\end{aligned}$$

As in the 1-D case, we desingularize the velocities u and v by setting

$$u=\frac{\sqrt{2}h^2u}{\sqrt{h^4+\max\{h^4,\varepsilon\}}}\quad\text{and}\quad v=\frac{\sqrt{2}h^2v}{\sqrt{h^4+\max\{h^4,\varepsilon\}}}$$

at the centers of cell edges. As before, ε is a very small number. Following this, we recompute the corresponding point values of the discharges by setting $\boldsymbol{q}=h\cdot\boldsymbol{u}$.

Finally, the source term should be discretized in such a way which will result in a well-balanced central-upwind scheme. We use the quadrature developed in [22]; see also [2, 6, 33]. The first component of the source term is trivial and $\mathcal{S}^{(1)}_{j,k}=0$. The second component of the discrete source term is

$$\mathcal{S}^{(2)}_{j,k}=\frac{g}{|C_{j,k}|}\left[I^{(2)}_{j,k}-II^{(2)}_{j,k}\right],$$

where

$$\begin{aligned}I^{(2)}_{j,k}=&\frac{\ell_{j+\frac12,k}}{2}\cos\left(\theta_{j+\frac12,k}\right)\left(w^{\rm E}_{j,k}-B_{j+\frac12,k}\right)^2-\frac{\ell_{j-\frac12,k}}{2}\cos\left(\theta_{j-\frac12,k}\right)\left(w^{\rm W}_{j,k}-B_{j-\frac12,k}\right)^2\\&+\frac{\ell_{j,k+\frac12}}{2}\cos\left(\theta_{j,k+\frac12}\right)\left(w^{\rm N}_{j,k}-B_{j,k+\frac12}\right)^2-\frac{\ell_{j,k-\frac12}}{2}\cos\left(\theta_{j,k-\frac12}\right)\left(w^{\rm S}_{j,k}-B_{j,k-\frac12}\right)^2\end{aligned}$$

and

$$II^{(2)}_{j,k} = (\overline{w}_{j,k} - B_{j,k}) \Big[w^{\mathrm{E}}_{j,k} \ell_{j+\frac{1}{2},k} \cos\left(\theta_{j+\frac{1}{2},k}\right) + w^{\mathrm{W}}_{j,k} \ell_{j-\frac{1}{2},k} \cos\left(\theta_{j-\frac{1}{2},k}\right) + w^{\mathrm{N}}_{j,k} \ell_{j,k+\frac{1}{2}} \cos\left(\theta_{j,k+\frac{1}{2}}\right) + w^{\mathrm{S}}_{j,k} \ell_{j,k-\frac{1}{2}} \cos\left(\theta_{j,k-\frac{1}{2}}\right) \Big].$$

Similarly, the third component of the discrete source term is

$$\mathcal{S}^{(3)}_{j,k} = \frac{g}{|C_{j,k}|} \left[I^{(3)}_{j,k} - II^{(3)}_{j,k} \right],$$

where

$$I^{(3)}_{j,k} = \frac{\ell_{j+\frac{1}{2},k}}{2} \sin\left(\theta_{j+\frac{1}{2},k}\right) \left(w^{\mathrm{E}}_{j,k} - B_{j+\frac{1}{2},k} \right)^2 - \frac{\ell_{j-\frac{1}{2},k}}{2} \sin\left(\theta_{j-\frac{1}{2},k}\right) \left(w^{\mathrm{W}}_{j,k} - B_{j-\frac{1}{2},k} \right)^2 + \frac{\ell_{j,k+\frac{1}{2}}}{2} \sin\left(\theta_{j,k+\frac{1}{2}}\right) \left(w^{\mathrm{N}}_{j,k} - B_{j,k+\frac{1}{2}} \right)^2 - \frac{\ell_{j,k-\frac{1}{2}}}{2} \sin\left(\theta_{j,k-\frac{1}{2}}\right) \left(w^{\mathrm{S}}_{j,k} - B_{j,k-\frac{1}{2}} \right)^2$$

and

$$II^{(3)}_{j,k} = (\overline{w}_{j,k} - B_{j,k}) \Big[w^{\mathrm{E}}_{j,k} \ell_{j+\frac{1}{2},k} \sin\left(\theta_{j+\frac{1}{2},k}\right) + w^{\mathrm{W}}_{j,k} \ell_{j-\frac{1}{2},k} \sin\left(\theta_{j-\frac{1}{2},k}\right) + w^{\mathrm{N}}_{j,k} \ell_{j,k+\frac{1}{2}} \sin\left(\theta_{j,k+\frac{1}{2}}\right) + w^{\mathrm{S}}_{j,k} \ell_{j,k-\frac{1}{2}} \sin\left(\theta_{j,k-\frac{1}{2}}\right) \Big].$$

4 One-Dimensional/Two-Dimensional Coupling

⟨bc⟩ Correctly coupling the reaches to the confluence region is perhaps the crucial part of the proposed method. We follow the ideas from [34, 40]. Recall our notation: A superscript $(\cdot)^{(R_i)}$ indicates a value corresponds to the ith reach; no superscript indicates a value corresponds to the confluence region D.

The boundary condition for reach R_i at the end connecting to the confluence region is given by

$$\boldsymbol{U}^{(R_i)}\big|_{\partial D} = \frac{1}{|\partial D_{R_i}|} \int\limits_{\partial D_{R_i}} \boldsymbol{\mathcal{U}}\, ds, \tag{4.1}$$ bc1

where ∂D denotes the boundary of the confluence region D and ∂D_{R_i} denotes the edge that corresponds to the side on which reach R_i enters the river junction. The boundary condition for the confluence region on that side is

$$\boldsymbol{\mathcal{U}}|_{\partial D_{R_i}} = \boldsymbol{U}^{(R_i)}\big|_{\partial D}. \tag{4.2}$$ bc2

We stress that (4.1) implies that $\boldsymbol{U}^{(R_i)}$ at the end that connects to the confluence region takes the average value of $\boldsymbol{\mathcal{U}}$ along the edge on the side of R_i, while (4.2) sets the value of $\boldsymbol{\mathcal{U}}$ all along the edge of D corresponding to R_i to be the end value of $\boldsymbol{U}^{(R_i)}$.

In addition, along the edge of D that does not correspond to a reach, a solid wall boundary condition is enforced of $\boldsymbol{u} \cdot \boldsymbol{n} = 0$.

In the remaining part of this section, we provide details on implementing these connecting boundary conditions. The description consists of the following three stages: assignment of ghost cell averages, reconstruction of boundary cells and assignment of ghost cell edge values.

4.1 Ghost Cell Averages

⟨sec41⟩ For the ghost cells on three sides of D, we assign the cell average values corresponding to the values found at the end of the corresponding reach connected to D as shown in Figure 2.2. To this end, one has to be careful about matching the direction of flow in the ghost cells with the direction of the reach relative to D. Furthermore, the integral in (4.1) will be computed using the midpoint rule, so it becomes an area-weighted average.

The ghost cell averages for the reaches are then assigned as follows.

1. At the downstream end of R_1, we set

$$\overline{\boldsymbol{U}}_{N_1+1}^{(R_1)} = \left(\frac{\sum_{k=1}^{M}|C_{1,k}|\overline{h}_{1,k}}{\sum_{k=1}^{M}|C_{1,k}|}, \frac{\sum_{k=1}^{M}|C_{1,k}|\overline{(hu)}_{1,k}}{\sum_{k=1}^{M}|C_{1,k}|}\right)^{\top}.$$

2. At the downstream end of R_2, we set

$$\overline{\boldsymbol{U}}_{N_2+1}^{(R_2)} = \left(\frac{\sum_{j=1}^{M}|C_{j,1}|\overline{h}_{j,1}}{\sum_{j=1}^{M}|C_{j,1}|}, \frac{\sum_{j=1}^{M}|C_{j,1}|\overline{(hu)}_{j,1}}{\sum_{j=1}^{M}|C_{j,1}|}\cos\phi + \frac{\sum_{j=1}^{M}|C_{j,1}|\overline{(hv)}_{j,1}}{\sum_{j=1}^{M}|C_{j,1}|}\sin\phi\right)^{\top}.$$

3. At the upstream end of R_3, we set

$$\overline{\boldsymbol{U}}_{0}^{(R_3)} = \left(\frac{\sum_{k=1}^{M}|C_{M,k}|\overline{h}_{M,k}}{\sum_{k=1}^{M}|C_{M,k}|}, \frac{\sum_{k=1}^{M}|C_{M,k}|\overline{(hu)}_{M,k}}{\sum_{k=1}^{M}|C_{M,k}|}\right)^{\top}.$$

The ghost cell averages for the confluence region corresponding to inflow or outflow boundaries are assigned as follows.

1. At the left edge of D (corresponding to R_1), we set

$$\overline{\boldsymbol{\mathcal{U}}}_{0,k} = \left(\overline{h}_{N_1}^{(R_1)}, \overline{q}_{N_1}^{(R_1)}, 0\right)^{\top}, \quad k = 1, \ldots, M.$$

2. At the lower edge of D (corresponding to R_2), we set

$$\overline{\boldsymbol{\mathcal{U}}}_{j,0} = \left(\overline{h}_{N_2}^{(R_2)}, \overline{q}_{N_2}^{(R_2)}\cos\phi, \overline{q}_{N_2}^{(R_2)}\sin\phi\right)^{\top}, \quad j = 1, \ldots, M.$$

3. At the right edge of D (corresponding to R_3), we set

$$\overline{\boldsymbol{\mathcal{U}}}_{M+1,k} = \left(\overline{h}_{1}^{(R_3)}, \overline{q}_{1}^{(R_3)}, 0\right)^{\top}, \quad k = 1, \ldots, M.$$

An example of the assignment of ghost cell averages on the left side of D is shown in Figure 4.1.

For the fourth (upper) edge of D, we enforce a reflecting (solid wall) condition, which results in the following formulae:

$$\overline{h}_{j,M+1} = \overline{h}_{j,M}, \quad \overline{\boldsymbol{q}}_{j,M+1} = \overline{\boldsymbol{q}}_{j,M} - 2(\overline{\boldsymbol{q}}_{j,M}\cdot\boldsymbol{n})\boldsymbol{n}, \tag{4.3}$$ 4.3

where $\boldsymbol{n}$ is the unit outward normal vector in the direction of the ghost cell. In the coordinate form, formula (4.3) reads as

$$\overline{\boldsymbol{\mathcal{U}}}_{j,M+1} = \begin{pmatrix} \overline{h}_{j,M} \\ -\overline{(hu)}_{j,M}\cos(2\phi) + \overline{(hv)}_{j,M}\sin(2\phi) \\ \overline{(hu)}_{j,M}\sin(2\theta_{j,m+\frac{1}{2}}) + \overline{(hv)}_{j,M}\cos(2\theta_{j,m+\frac{1}{2}}) \end{pmatrix}, \quad j = 1, \ldots, M.$$

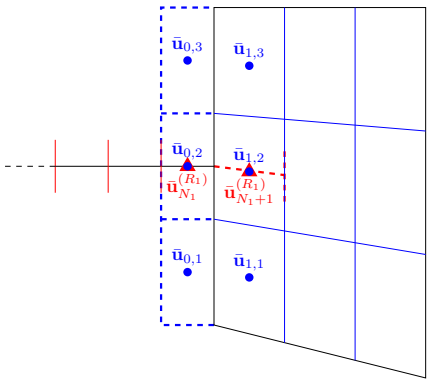

Figure 4.1: Assignment of ghost cells between a reach and the confluence region.

4.2 Boundary Point Values

Equipped with the ghost cell averages obtained in §4.1, we now compute the boundary point values required to evolve the solution on both sides of ∂D.

To this end, we need to complete the piecewise linear reconstruction in the cells adjusted to ∂D both in the 1-D reached and inside the confluence domain D. We begin with the boundary cells of the 1-D reaches. It should be observed that the 1-D grid is not uniform there since the size of the ghost cells is not necessarily equal to Δx. Therefore, one cannot directly apply the reconstructed procedure (3.1)–(3.4) as the computation of the slopes in (3.3) must be modified. This is done in three different reaches as follows.

1. At the downstream end of R_1, we set

$$(\boldsymbol{P}_x)^{(R_1)}_{N_1} = \text{minmod}\left(\kappa\frac{2\big(\overline{\boldsymbol{V}}^{(R_1)}_{N_1+1}-\overline{\boldsymbol{V}}^{(R_1)}_{N_1}\big)}{\Delta x+\Delta x^{(R_1)}_{N_1+1}},\ \frac{2\big(\overline{\boldsymbol{V}}^{(R_1)}_{N_1+1}-\overline{\boldsymbol{V}}^{(R_1)}_{N_1-1}\big)}{3\Delta x+\Delta x^{(R_1)}_{N_1+1}},\ \kappa\frac{\overline{\boldsymbol{V}}^{(R_1)}_{N_1}-\overline{\boldsymbol{V}}^{(R_1)}_{N_1-1}}{\Delta x}\right). \quad (4.4)$$

2. At the downstream end of R_2, we set

$$(\boldsymbol{P}_x)^{(R_2)}_{N_2} = \text{minmod}\left(\kappa\frac{2\big(\overline{\boldsymbol{V}}^{(R_2)}_{N_2+1}-\overline{\boldsymbol{V}}^{(R_2)}_{N_2}\big)}{\Delta x+\Delta x^{(R_2)}_{N_2+1}},\ \frac{2\big(\overline{\boldsymbol{V}}^{(R_2)}_{N_2+1}-\overline{\boldsymbol{V}}^{(R_2)}_{N_2-1}\big)}{3\Delta x+\Delta x^{(R_2)}_{N_2+1}},\ \kappa\frac{\overline{\boldsymbol{V}}^{(R_2)}_{N_2}-\overline{\boldsymbol{V}}^{(R_2)}_{N_2-1}}{\Delta x}\right). \quad (4.5)$$

3. At the upstream end of R_3, we set

$$(\boldsymbol{P}_x)^{(R_3)}_{1} = \text{minmod}\left(\kappa\frac{\overline{\boldsymbol{V}}^{(R_3)}_{2}-\overline{\boldsymbol{V}}^{(R_3)}_{1}}{\Delta x},\ \frac{2\big(\overline{\boldsymbol{V}}^{(R_3)}_{2}-\overline{\boldsymbol{V}}^{(R_3)}_{0}\big)}{3\Delta x+\Delta x^{(R_3)}_{0}},\ \kappa\frac{2\big(\overline{\boldsymbol{V}}^{(R_3)}_{1}-\overline{\boldsymbol{V}}^{(R_3)}_{0}\big)}{\Delta x+\Delta x^{(R_3)}_{0}}\right). \quad (4.6)$$

We then calculate the boundary point values $\big(\boldsymbol{V}^-_{N_1+\frac12}\big)^{(R_1)}$, $\big(\boldsymbol{V}^-_{N_2+\frac12}\big)^{(R_2)}$ and $\big(\boldsymbol{V}^+_{\frac12}\big)^{(R_3)}$ by substituting (4.4), (4.5) and (4.6), respectively, into (3.1), (3.2) and (3.4), and obtain the corresponding values of $\big(\boldsymbol{U}^-_{N_1+\frac12}\big)^{(R_1)}$, $\big(\boldsymbol{U}^-_{N_2+\frac12}\big)^{(R_2)}$ and $\big(\boldsymbol{U}^+_{\frac12}\big)^{(R_3)}$ by using the relation $h=w-B$.

Next, we obtain point values at the boundary cells of the confluence region, namely, we compute $\boldsymbol{\mathcal{U}}^{\mathrm{W}}_{1,k}$, $\boldsymbol{\mathcal{U}}^{\mathrm{E}}_{M,k}$ for $k=1,\ldots,M$ and $\boldsymbol{\mathcal{U}}^{\mathrm{S}}_{j,1}$, $\boldsymbol{\mathcal{U}}^{\mathrm{N}}_{j,M}$ for $j=1,\ldots,M$, using the piecewise

linear reconstructions in the 2-D cells along ∂D, which are obtained precisely as explained in §3.2.

In order to compute the remaining point values, we would need to perform the data exchange between the 1-D and 2-D settings (similarly to what has been done to compute the ghost cell averages in §4.1).

The boundary point values for the 1-D reaches are assigned as follows (note that here instead of using area-weighted averages as was done in §4.1, we use side-length weighted averages).

1. At the downstream end of R_1, we set

$$\big(\boldsymbol{U}^+_{N_1+\frac{1}{2}}\big)^{(R_1)}=\left(\frac{\sum_{k=1}^M \ell_{\frac{1}{2},k}h^{\rm W}_{1,k}}{\sum_{k=1}^M \ell_{\frac{1}{2},k}},\frac{\sum_{k=1}^M \ell_{\frac{1}{2},k}\,(hu)^{\rm W}_{1,k}}{\sum_{k=1}^M \ell_{\frac{1}{2},k}}\right)^\top.$$

2. At the downstream end of R_2, we set

$$\big(\boldsymbol{U}^+_{N_2+\frac{1}{2}}\big)^{(R_2)}=\left(\frac{\sum_{j=1}^M \ell_{j,\frac{1}{2}}h^{\rm S}_{j,1}}{\sum_{j=1}^M \ell_{j,\frac{1}{2}}},\frac{\sum_{j=1}^M \ell_{j,\frac{1}{2}}\,(hu)^{\rm S}_{j,1}}{\sum_{j=1}^M \ell_{j,\frac{1}{2}}}\cos\phi+\frac{\sum_{j=1}^M \ell_{j,\frac{1}{2}}\,(hv)^{\rm S}_{j,1}}{\sum_{j=1}^M \ell_{j,\frac{1}{2}}}\sin\phi\right)^\top.$$

3. At the upstream end of R_3, we set

$$\big(\boldsymbol{U}^-_{\frac{1}{2}}\big)^{(R_3)}=\left(\frac{\sum_{k=1}^M \ell_{M+\frac{1}{2},k}h^{\rm E}_{M,k}}{\sum_{k=1}^M \ell_{M+\frac{1}{2},k}},\frac{\sum_{k=1}^M \ell_{M+\frac{1}{2},k}\,(hu)^{\rm E}_{M,k}}{\sum_{k=1}^M \ell_{M+\frac{1}{2},k}}\right)^\top.$$

The point values at the inflow or outflow boundaries of the confluence region are assigned as follows.

1. At the left edge of D (corresponding to R_1), we set

$$\boldsymbol{\mathcal{U}}^{\rm E}_{0,k}=\Big(\big(h^-_{N_1+\frac{1}{2}}\big)^{(R_1)},\big(q^-_{N_1+\frac{1}{2}}\big)^{(R_1)},0\Big)^\top,\quad k=1,\ldots,M.$$

2. At the lower edge of D (corresponding to R_2), we set

$$\boldsymbol{\mathcal{U}}^{\rm N}_{j,0}=\Big(\big(h^-_{N_2+\frac{1}{2}}\big)^{(R_2)},\big(q^-_{N_2+\frac{1}{2}}\big)^{(R_2)}\cos\phi,\big(q^-_{N_2+\frac{1}{2}}\big)^{(R_2)}\sin\phi\Big)^\top,\quad j=1,\ldots,M.$$

3. At the right edge of D (corresponding to R_3), we set

$$\boldsymbol{\mathcal{U}}^{\rm W}_{M+1,k}=\Big(\big(h^+_{\frac{1}{2}}\big)^{(R_3)},\big(q^+_{\frac{1}{2}}\big)^{(R_3)},0\Big)^\top,\quad k=1,\ldots,M.$$

Finally, at the fourth (upper) edge of D, corresponding to a reflecting (solid wall) boundary condition, we set

$$\boldsymbol{\mathcal{U}}^{\rm S}_{j,M+1}=\begin{pmatrix}h^{\rm N}_{j,M}\\ -(hu)^{\rm N}_{j,M}\cos(2\phi)+(hv)^{\rm N}_{j,M}\sin(2\phi)\\ (hu)^{\rm N}_{j,M}\sin(2\theta_{j,m+\frac{1}{2}})+(hv)^{\rm N}_{j,M}\cos(2\theta_{j,m+\frac{1}{2}})\end{pmatrix},\quad j=1,\ldots,M.$$

5 Numerical Examples

⟨sec6⟩ In this section, we test the developed 1-D/2-D coupling approach on a number of numerical examples in which the semi-discrete systems (3.5) and (3.8) are integrated in time using the three-stage third-order strong-stability preserving (SSP) Runge-Kutta solver; see, e.g., [12, 13]. In the following tests, we take the parameters:

$$g = 1, \quad \kappa = 1.5, \quad \varepsilon = (\Delta x)^4$$

unless specified otherwise. The results obtained using the 1-D/2-D coupling model are compared with reference solutions computed by a fully 2-D numerical method from [26] over triangular meshes.

Example 1—Shock wave through T-shaped junction

In this example, we consider the case where the tributary perpendicularly ($\phi = \pi/2$) enters the principal river with constant width. The confluence region is thus rectangular. The width of upstream (R_1) and downstream (R_3) reaches are $b_1 = b_3 = 0.2$, while the width of the tributary (R_2) is $b_2 = 0.1$. The nonflat bottom topography is defined by

$$B(x,y) = \begin{cases} 0.099 - 0.02(x+5), & \text{if } x < -0.05 \text{ in } R_1, \\ 0.1e^{-1.2(x-2.5)^2}, & \text{if } x > 0.05 \text{ in } R_3, \\ 0, & \text{otherwise.} \end{cases} \tag{5.1}$$ testbt1

The initial conditions corresponding to a dam-break flow are given by

$$w(x,y,0) = \begin{cases} 1.0, & \text{if } x < -0.5 \text{ in } R_1, \\ 0.5, & \text{otherwise,} \end{cases} \qquad u(x,y,0) = v(x,y,0) = 0. \tag{5.2}$$ ic1

We set outflow boundary conditions at every reach end not connected to the river junction. The computational domain, the initial water level $w(x,y,t=0)$ as well as the water level $w(x,y,t=4)$ computed by the fully 2-D scheme over a fine triangular mesh with 58818 cells are shown in Figure 5.1.

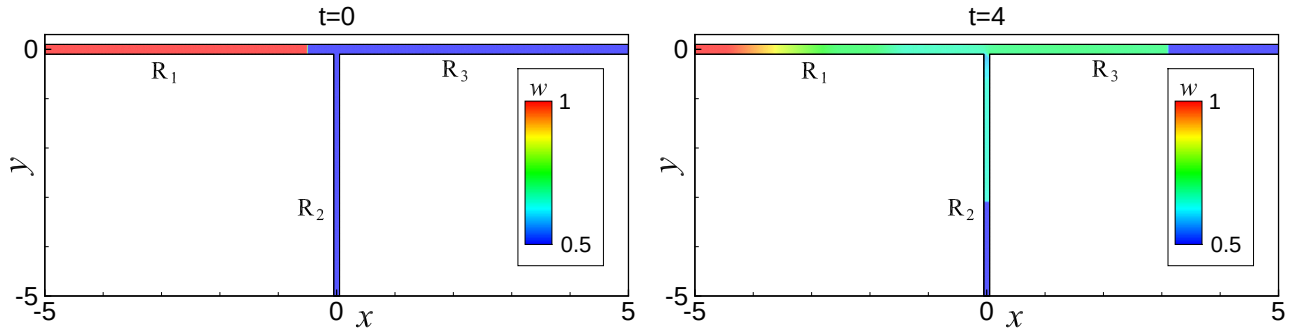

Figure 5.1: Example 1: Initial (left) and simulated (right) water surface w.

Using the proposed numerical model, each reach is discretized by 1-D cells with the mesh size $\Delta x = 0.1$ and the confluence region is discretized using $M \times M$ cells. In Figures 5.2 and

5.3, we compare the water surface w and discharge hu computed at $t = 4$ in all three reaches using the proposed 1-D/2-D coupling approach (with $M = 4$ and 16) with the corresponding horizontal cross-section averaged quantities estimated using the 2-D model. One can see that despite the discrepancy near the conjunction area, the 1-D/2-D results are in a good agreement with the fully 2-D results in all three reaches in terms of water levels and front positions of the waves. One can also clearly observe that using the finer mesh in the confluence region ($M = 16$) in the 1-D/2-D coupling model will lead to a better agreement with the 2-D results. In addition, one may observe larger differences between the presented results in the confluence region. In order to further investigate this, we show Figure 5.4 in which we plot the water surface contours and velocity vectors computed using the fully 2-D scheme. One can clearly see that when the dam-break flow enters the confluence region, strong 2-D features are generated there. Moreover, a vortex is clearly formed in the tributary R_2 so that the 2-D features in reach R_2 are stronger than in the main river (reaches R_1 and R_3).

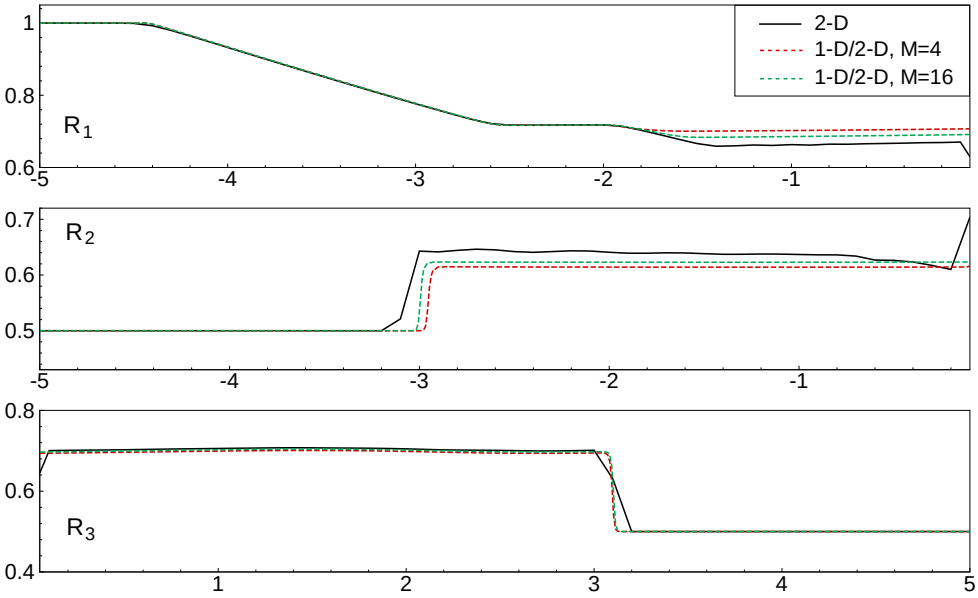

Figure 5.2: Example 1: Comparison of the water surface w in reaches R_1, R_2 and R_3 computed at $t = 4$ using the proposed 1-D/2-D coupling model with the averaged water levels from the 2-D computations.

⟨rFig2⟩

Example 2—Shock wave through junction with $\phi = \pi/3$ tributary angle

In the second example, we consider a different geometrical setting, in which the tributary enters the principal river at angle $\phi = \pi/3$ and the side lengths are $b_1 = 0.2$, $b_2 = 0.1/\sin\phi$, and $b_3 = 0.2(1+\cot\phi)$. The bottom topography function and initial data are still given by (5.1) and (5.2), respectively. As in Example 1, we set outflow boundary conditions at every reach end not connected to the river junction. In Figure 5.5, we plot the computational domain, the initial water level $w(x, y, t = 0)$ and the water level $w(x, y, t = 4)$ computed by the fully 2-D scheme over a fine triangular mesh with 91729 cells.

Once again, each reach is discretized by 1-D cells with the mesh size $\Delta x = 0.1$ and the confluence region is discretized using $M \times M$ cells. In Figures 5.6 and 5.7, we compare the

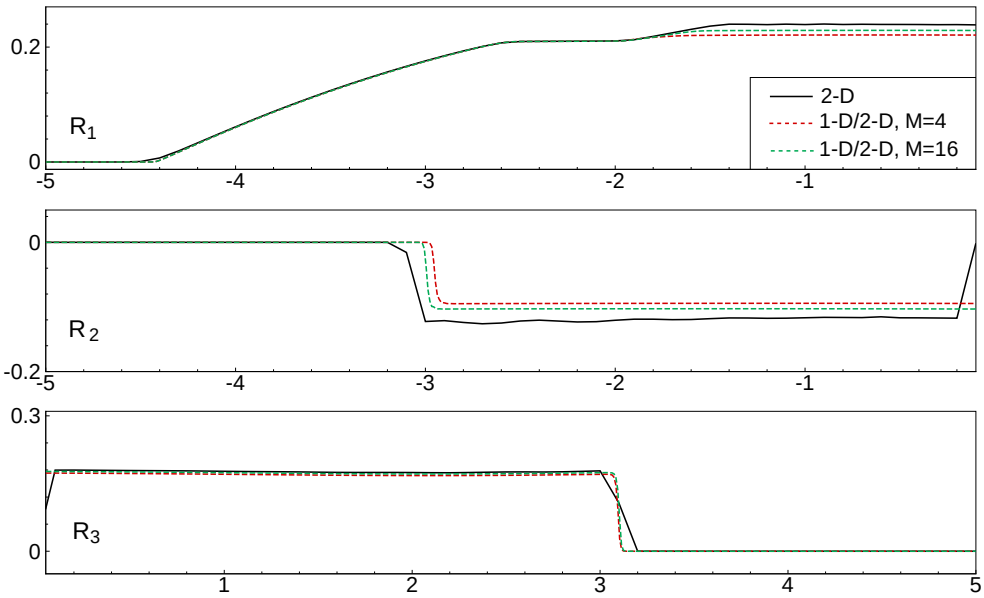

Figure 5.3: Example 1: Comparison of the flow discharge hu in reaches R_1, R_2 and R_3 computed at $t = 4$ using the proposed 1-D/2-D coupling model with the corresponding averaged flow discharges from the 2-D computations.

⟨rFig3⟩

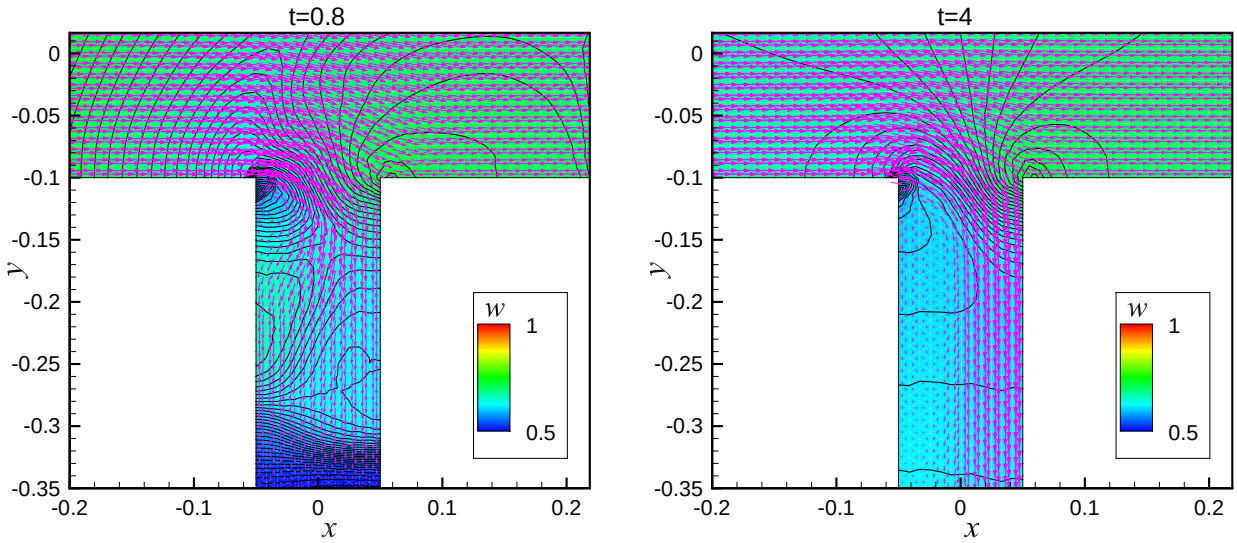

Figure 5.4: Example 1: Velocity vectors and contour lines of w computed at times $t = 0.8$ (left) and 4 (right) by the fully 2-D scheme—zoom at the confluence region.

⟨rFig4⟩

water surface w and discharge hu computed at $t = 4$ in all three reaches using the proposed 1-D/2-D coupling approach (with $M = 4$, 16 and 32) with the corresponding horizontal cross-section averaged quantities estimated using the 2-D model. As one can see, the use of a finer mesh in the confluence region leads to a better agreement between the 1-D/2-D results and the fully 2-D results in all three reaches in terms of water levels and front positions of the waves. As before, one may observe larger differences between the presented results in the confluence region due to strong 2-D features and vortices are generated when the dam-break flow enters

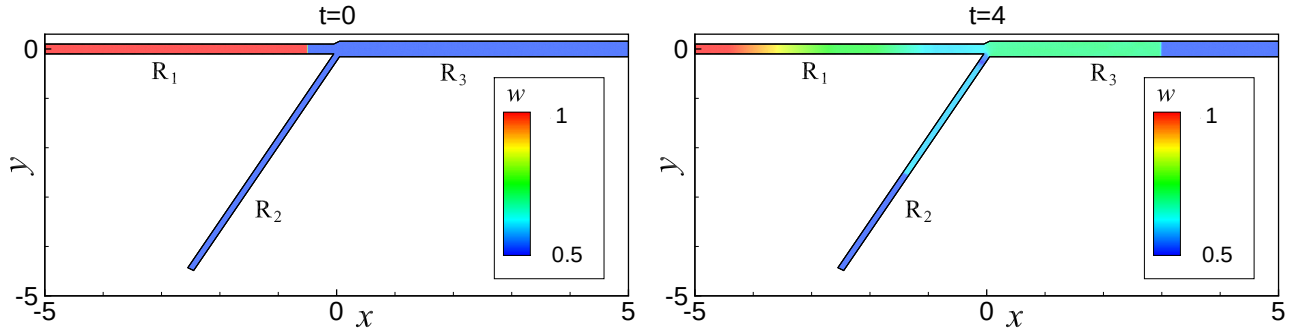

Figure 5.5: Example 2: Initial (left) and simulated (right) water surface w.

there; see Figure 5.8, where we plot the water surface contours and velocity vectors computed using the fully 2-D scheme.

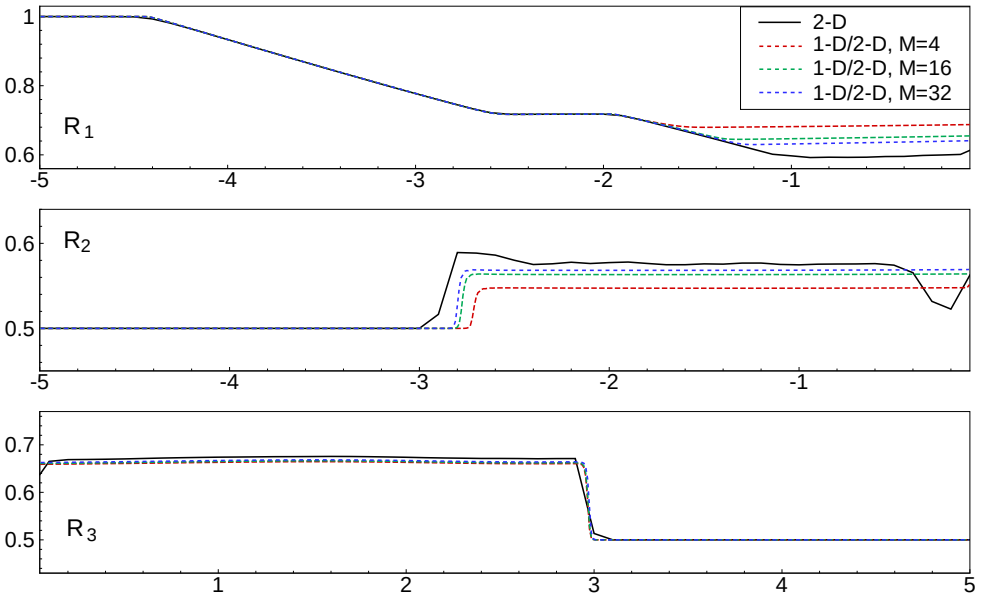

Figure 5.6: Example 2: Comparison of the water surface w in reaches R_1, R_2 and R_3 computed at $t = 4$ using the proposed 1-D/2-D coupling model with the averaged water levels from the 2-D computations.

⟨t2Fig2⟩

Example 3—Steady flow through junction with $\phi = \pi/3$ tributary angle

In this test, we consider steady flows in the same computational domain as in Example 2. The nonflat bottom topography is defined by

$$B(x,y) = \begin{cases} 0.04e^{-2(x+2.5)^2}, & \text{if } x < -0.05 \text{ in } R_1, \\ 0.05e^{-2(x-2.5)^2}, & \text{if } x > 0.05 \text{ in } R_3, \\ 0, & \text{otherwise,} \end{cases}$$

and the initial data are

$$w(x,y,0) \equiv 0.5, \quad u(x,y,0) = v(x,y,0) \equiv 0.$$

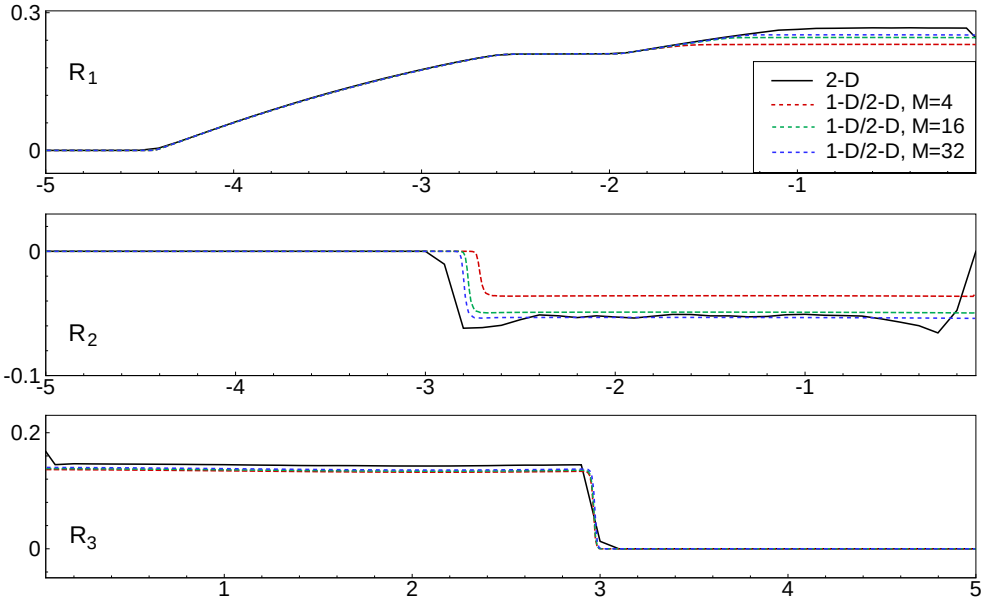

Figure 5.7: Example 2: Comparison of the flow discharge hu in reachesR_1, R_2 and R_3 computed at $t = 4$ using the proposed 1-D/2-D coupling model with the corresponding averaged flow discharges from the 2-D computations.

⟨t2Fig3⟩

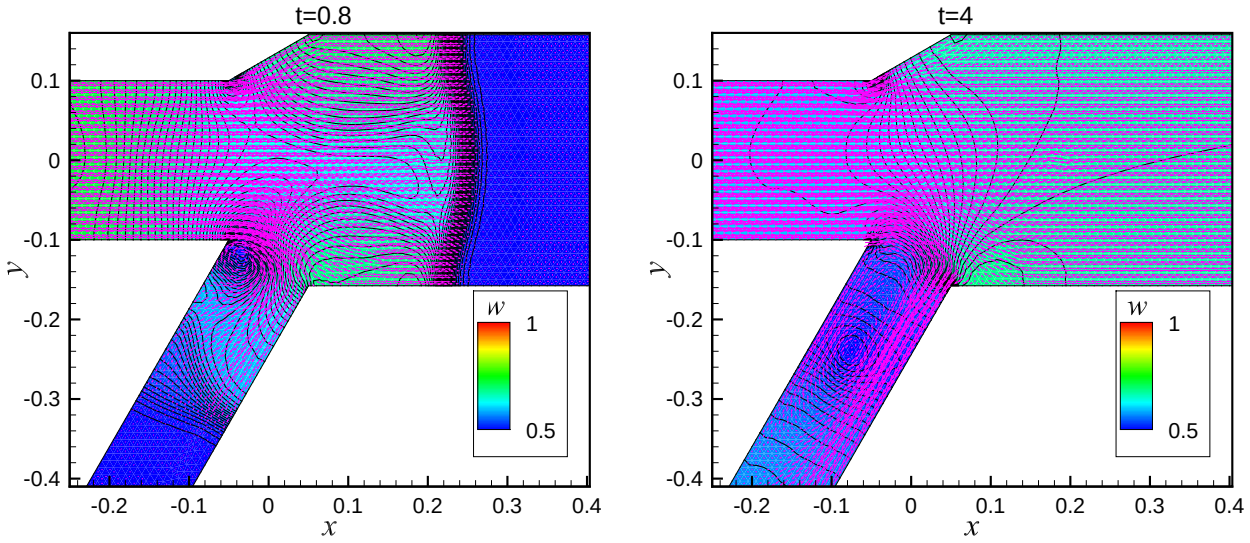

Figure 5.8: Example 2: Velocity vectors and contour lines of w computed at times $t = 0.8$ (left) and 4 (right) by the fully 2-D scheme—zoom at the confluence region.

⟨t2Fig4⟩

The inflow boundary condition is given by $hu = 0.2$ for the R_1 reach, $hu = 0.1$ for the R_2 reach (tributary), and the outflow boundary condition is set to be $w = 0.48$ for the R_3 reach. The gravitational acceleration $g = 9.81$ is used in this experiment.

We run both the 1-D/2-D and fully 2-D simulations until the final time $t = 800$ when the flow reaches the steady state. The 1-D/2-D results are obtained using a uniform mesh with $\Delta x = 0.1$ in each reach and $M \times M$ cells in the confluence region (with $M = 4$, 16 and 32). The fully 2-D simulations are performed on a triangular mesh with 11983 cells. The obtained results

are compared in Figures 5.9 and 5.10 demonstrating that both models approach similar steady states as expected. In Figure 5.9, one can clearly observe that the steady state solutions in R_1 and R_2 are affected by the 2-D flow structures in the confluence region and a higher resolution within the confluence region (larger M) leads to a better agreement with the fully 2-D model.

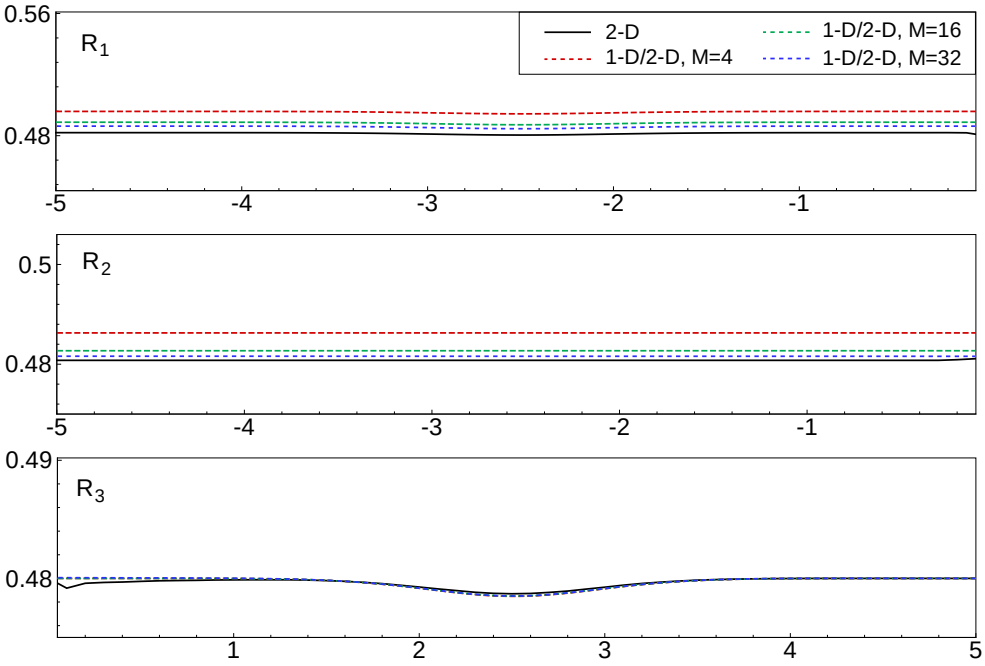

Figure 5.9: Example 3: Comparison of the water surface w in reaches R_1, R_2 and R_3 computed at $t = 800$ using the proposed 1-D/2-D coupling model with the averaged water levels from the 2-D computations.

⟨t3Fig1⟩

Example 4—Accuracy test

In this example, we investigate the experimental convergence order of the proposed numerical method. We use the following settings. The width of upstream (R_1) and downstream (R_3) reaches are $b_1 = 0.2$ and $b_3 = 0.3$, while the width of the tributary (R_2) is $b_2 = 0.1$ and the tributary angle is $\phi = \pi/3$. Each reach has a length of 5. A flat bottom $B(x, y) \equiv 0$ is used over the entire domain and the smooth initial water surface and velocities are given by

$$w(x,0) = \begin{cases} 1 + 0.01\Big[1 - \cos\big(10\pi(x+0.4)\big)\Big], & \text{if } -0.4 < x < -0.2 \text{ in } R_1, \\ 1, & \text{otherwise,} \end{cases}$$

$$u(x,y,0) = v(x,y,0) \equiv 0.$$

Each reach is discretized using $N_1 = N_2 = N_3 = N$ grid cells and the confluence region is discretized by $M \times M$ cells. The area of the confluence region scales depending on $\Delta x = 5/N$. We set outflow boundary conditions at every reach end not connected to the river junction and compute the solution until the final time $t = 0.7$.

Tables 5.1 and 5.2 show the L^1-errors and experimental convergence rates of water surface w computed by the proposed numerical model with $M = 4$ and $M = 8$, respectively. The result

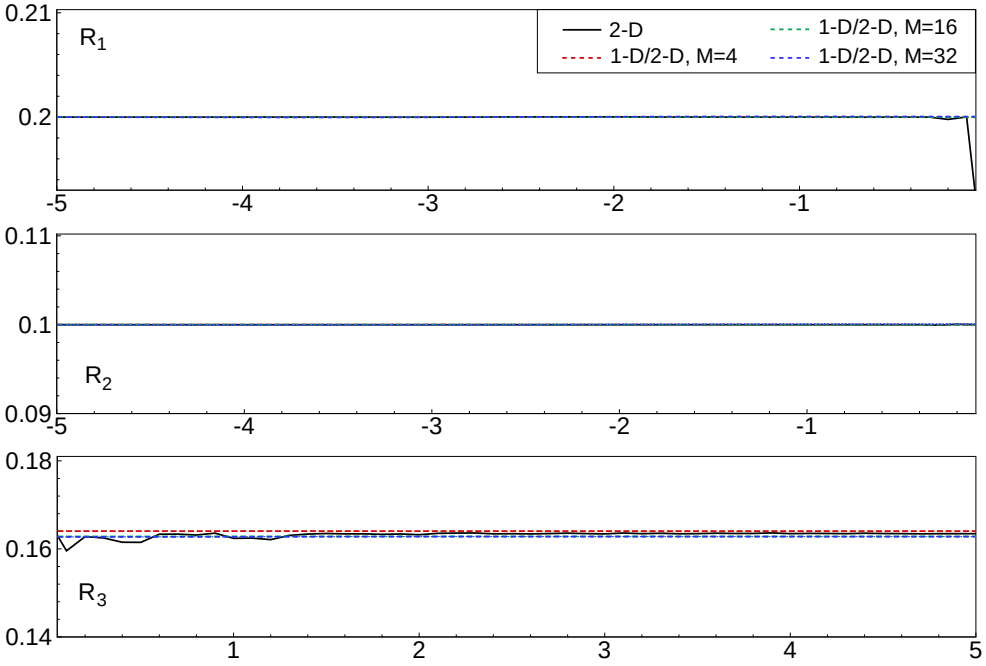

Figure 5.10: Example 3: Comparison of the flow discharge hu in reachesR_1, R_2 and R_3 computed at $t = 800$ using the proposed 1-D/2-D coupling model with the corresponding averaged flow discharges from the 2-D computations.

⟨t3Fig2⟩

computed with $N = 12800$ and $M = 8$ is used as a reference solution. One can observe that the proposed numerical method achieves the desired second order of accuracy in each reach as well as in the entire domain. In Figure 5.11, we illustrate the computed wave in each of the reaches for different values of N. One can clearly observe the self-convergence of the computed solution as the mesh is refined.

N	R_1		R_2		R_3		Entire Domain	
	L^1-error	Rate	L^1-error	Rate	L^1-error	Rate	L^1-error	Rate
200	2.63e-04	–	7.09e-05	–	1.84e-04	–	5.18e-04	–
400	6.33e-05	2.05	2.22e-05	1.68	5.91e-05	1.64	1.45e-04	1.84
800	1.23e-05	2.36	4.80e-06	2.21	1.36e-05	2.12	3.07e-05	2.24
1600	3.21e-06	1.94	1.22e-06	1.98	3.37e-06	2.02	7.80e-06	2.11
3200	5.32e-07	2.59	2.71e-07	2.17	7.51e-07	2.16	1.56e-06	2.32

Table 5.1: Example 4: L^1-errors and convergence rates for water surface w with $M = 4$.

Example 5—Supercritical shock wave through T-shaped junction

In this last example, we consider the case where the tributary perpendicularly ($\phi = \pi/2$) enters the principal river with constant width. The confluence region is thus rectangular. The width of upstream (R_1) and downstream (R_3) reaches are $b_1 = b_3 = 0.1$, while the width of the

Number of cells	R_1		R_2		R_3		Entire Domain	
	L^1-error	Rate	L^1-error	Rate	L^1-error	Rate	L^1-error	Rate
200	2.72e-04	–	1.07e-04	–	2.55e-04	–	6.34e-04	–
400	6.63e-05	2.04	4.05e-05	1.40	1.01e-04	1.34	2.08e-04	1.61
800	1.48e-05	2.16	1.25e-05	1.70	2.93e-05	1.79	5.66e-05	1.88
1600	3.50e-06	2.09	3.31e-06	1.92	7.29e-06	2.01	1.41e-05	2.01
3200	7.03e-07	2.31	7.27e-07	2.19	1.64e-06	2.15	3.07e-06	2.20

Table 5.2: Example 4: L^1-errors and convergence rates for water surface w with $M = 8$.

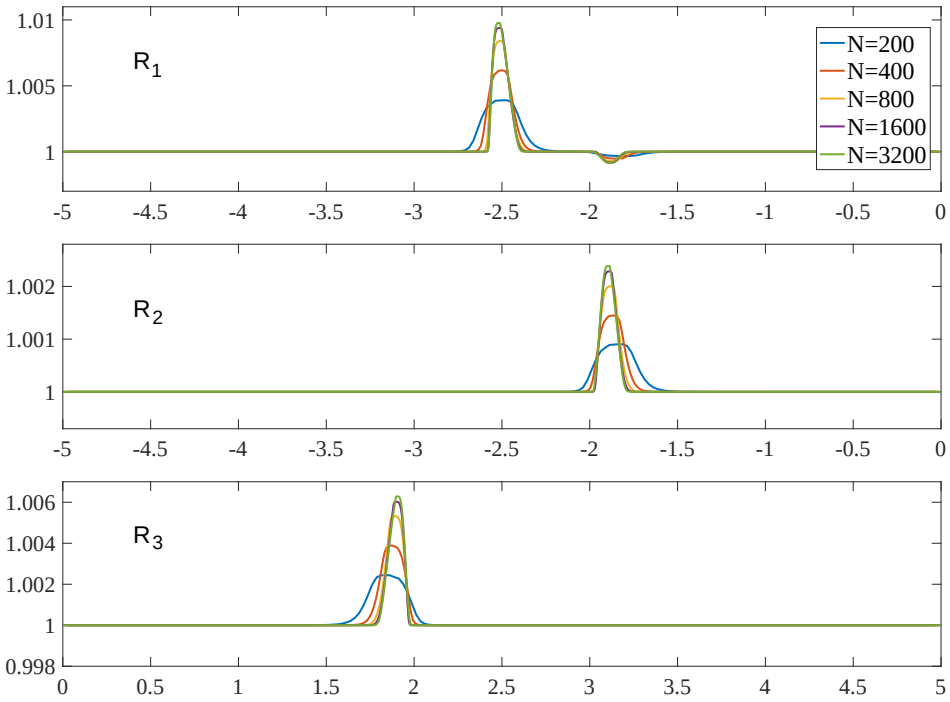

Figure 5.11: Example 4: Water surface w computed using the proposed model in each reach with $M = 4$ computed at $t = 0.7$.

⟨t4Fig1⟩

tributary (R_2) is $b_2 = 0.2$. The flat bottom $B(x, y) \equiv 0$ is used in this test and the initial conditions, which correspond to an isolated supercritical shock wave with the Froude number 1.135 initially propagating in the y-direction ($u(x, y, 0) \equiv 0$) in the tributary (R_2), are given by

$$w(x,y,0) = \begin{cases} 0.377, & \text{if } y < -1.5 \text{ in } R_2, \\ 0.1, & \text{otherwise,} \end{cases} \qquad v(x,y,0) = \begin{cases} 2.184, & \text{if } y < -1.5 \text{ in } R_2, \\ 0, & \text{otherwise.} \end{cases}$$

We set an inflow boundary conditions with $h = 0.377$ and $v = 2.184$ in reach R_2 at $y = -5$ and outflow boundary conditions at the ends of reaches R_1 and R_3 not connected to the river junction. The gravitational acceleration $g = 9.81$ is used in this test. The computational domain, the initial water level $w(x, y, t = 0)$ as well as the water level $w(x, y, t = 2)$ computed by the fully 2-D scheme over a fine triangular mesh with 41818 cells are shown in Figure 5.12.

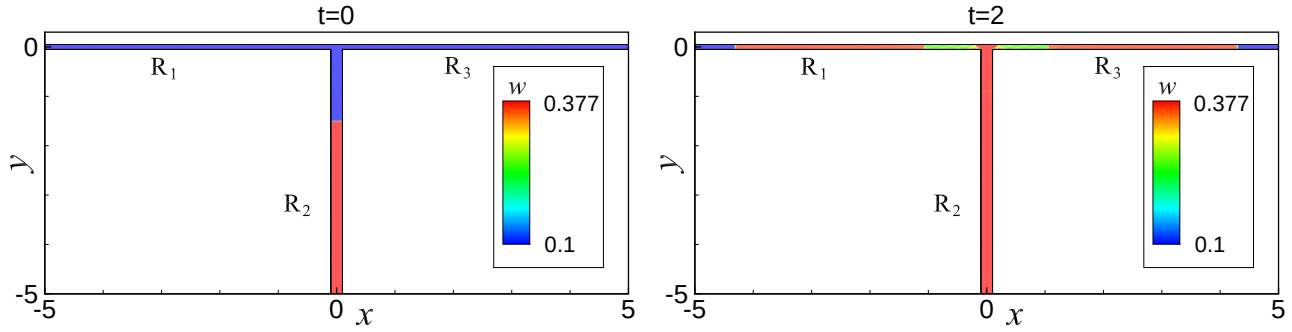

Figure 5.12: Example 5: Initial (left) and simulated (right) water surface w.

Using the proposed numerical model, each reach is discretized by 1-D cells with the mesh size $\Delta x = 0.1$ and the confluence region is discretized using $M \times M$ cells. In Figures 5.13 and 5.14, we compare the water surface w and discharge hu computed at $t = 2$ in reach R_3 using the proposed 1-D/2-D coupling approach (with $M = 16$ and 64) with the corresponding horizontal cross-section averaged quantities estimated using the 2-D model (we do not show the solutions in reaches R_1 and R_2 as the former one is symmetric to the solution in R_3 and the latter one is flat). Once again, despite quite large discrepancy near the conjunction area, the 1-D/2-D results are in a reasonably good agreement with the fully 2-D results in terms of water levels and front positions of the waves.

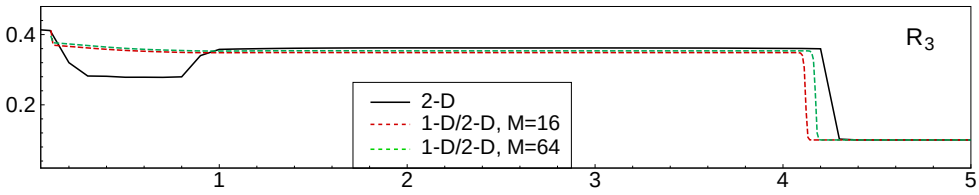

Figure 5.13: Example 5: Comparison of the water surface w in reach R_3 computed at $t = 2$ using the proposed 1-D/2-D coupling model with the averaged water levels from the 2-D computations.
⟨t5Fig2⟩

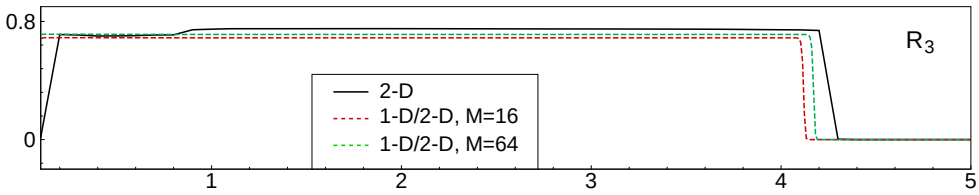

Figure 5.14: Example 5: Comparison of the flow discharge hu in reach R_3 computed at $t = 2$ using the proposed 1-D/2-D coupling model with the averaged flow discharge from the 2-D computations.
⟨t5Fig3⟩

Example 6—Dam-break wave transportation over steady flow through junction with $\phi = \pi/3$ tributary angle

In this test, we consider a large scale of the computational domain with a $\phi = \pi/3$ tributary angle. The nonflat bottom topography is defined by

$$B(x,y) = \begin{cases} 0.002(x+1.299), & \text{if } x < -1.299 \text{ in } R_1, \\ 0.01(y+4), & \text{if } y < -4 \text{ in } R_2, \\ 0.004(x-1.299), & \text{if } x > 1.299 \text{ in } R_3, \\ 0, & \text{otherwise,} \end{cases}$$

and the initial data are

$$w(x,y,0) \equiv 4, \quad u(x,y,0) = v(x,y,0) \equiv 0.$$

The inflow boundary conditions are given by $hu = -0.1$ for the R_3 reach and $w = 4$ for the R_2 reach (tributary), and the outflow boundary condition is set to be $w = 4$ for the R_1 reach. The gravitational acceleration $g = 9.81$ is used in this experiment.

The width of upstream (R_3) and downstream (R_1) reaches are $b_3 = 8$ and $b_1 = 5$, respectively, while the width of the tributary (R_2) is $b_2 = 3$. We run both the 1-D/2-D and fully 2-D simulations until the final time $t = 5000$, by which the flow converges to the steady state. The 1-D/2-D results are obtained using a uniform mesh with $\Delta x = 2.5$ in each reach and $M \times M$ cells in the confluence region with $M = 12$. The fully 2-D simulations are performed on a triangular mesh with 38080 cells.

The obtained steady state solutions are shown in Figures 5.15 and 5.16 demonstrating that both models approach similar steady states as expected.

Once the steady state results are obtained at $t = 5000$, we introduce a dam-break wave from the inflow boundary of the R_3 reach by setting $hu = -0.5$, and then simulate the wave transport until $t = 5023$. The results plotted in Figures 5.17 and 5.18 clearly indicate that the wave location computed by proposed numerical scheme agree well with those obtained by the full 2-D simulations. However, due to the strong 2-D flow structure in the conjunction area, some discrepancy of water height and discharge are observed in the tributary after the dam break wave passes the area.

6 Conclusion

⟨sec7⟩ In this paper, we have proposed a new 1-D/2-D coupling approach for modeling river systems. In the developed model, the flow in each reach of the river is governed by the 1-D Saint-Venant system of shallow water equations, while the full 2-D system is used in the confluence region, which is represented by a trapezoidal domain, whose dimensions are determined by the widths of the corresponding reaches, which are assumed to be constant for each reach. Both 1-D and 2-D systems are numerically solved by the well-balanced positivity preserving central-upwind schemes. The efficiency of the presented approach hinges upon the ability of using very coarse meshes inside the 2-D confluence region. A number of numerical experiments have been conducted to illustrate the robustness of the proposed modeling strategy.

Considering reaches of constant widths is somehow unrealistic and imposes certain limitations to the applicability of our model to the large scale river system computations. In the

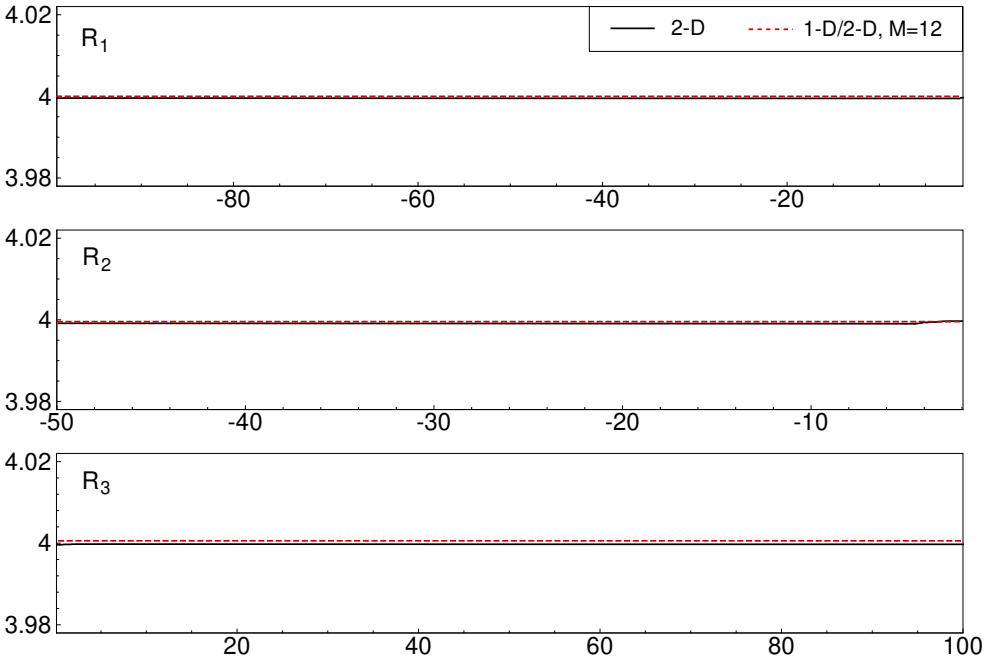

Figure 5.15: Example 6: Comparison of the water surface w in reaches R_1, R_2 and R_3 computed at $t = 5000$ using the proposed 1-D/2-D coupling model with the averaged water levels from the 2-D computations.

⟨t6Fig1⟩

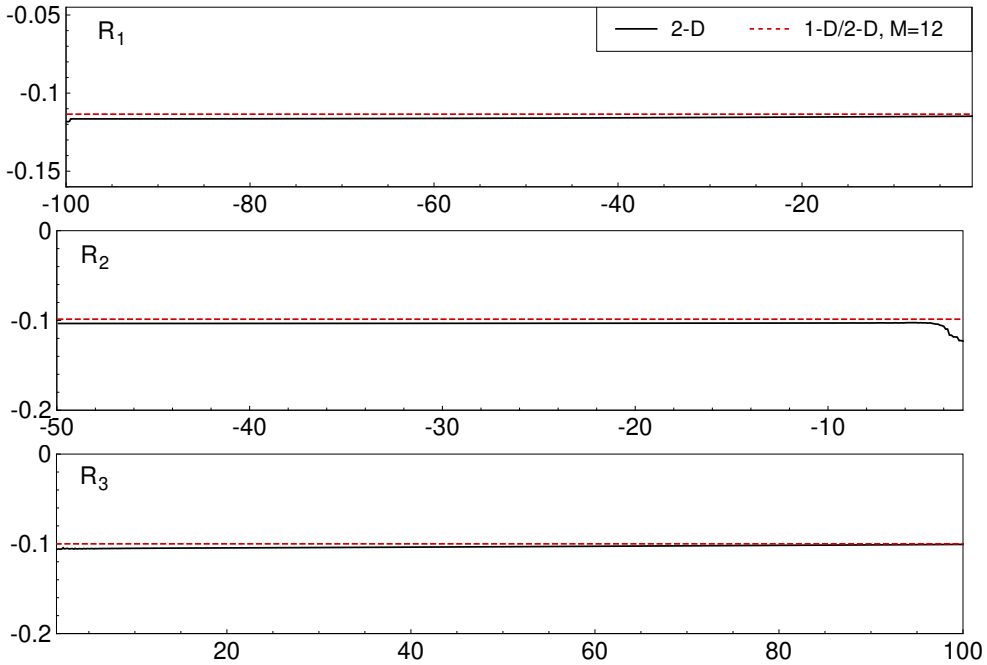

Figure 5.16: Example 6: Comparison of the flow discharge hu in reaches R_1, R_2 and R_3 computed at $t = 5000$ using the proposed 1-D/2-D coupling model with the averaged flow discharge from the 2-D computations.

⟨t6Fig2⟩

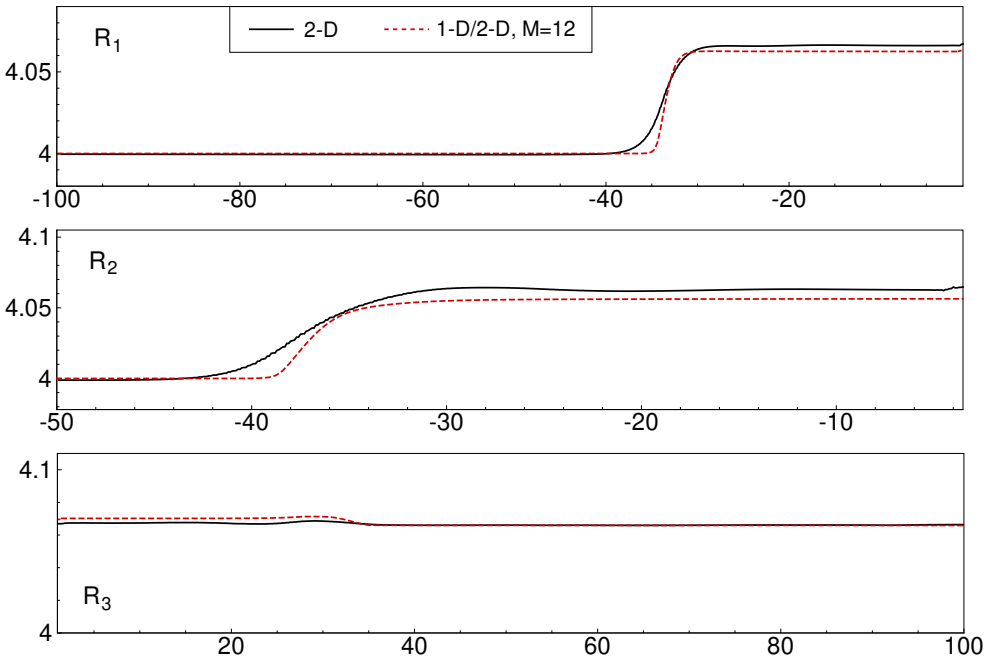

Figure 5.17: Example 6: Comparison of the water surface w in reaches R_1, R_2 and R_3 computed at $t = 5023$ using the proposed 1-D/2-D coupling model with the averaged water levels from the 2-D computations.

⟨t6Fig3⟩

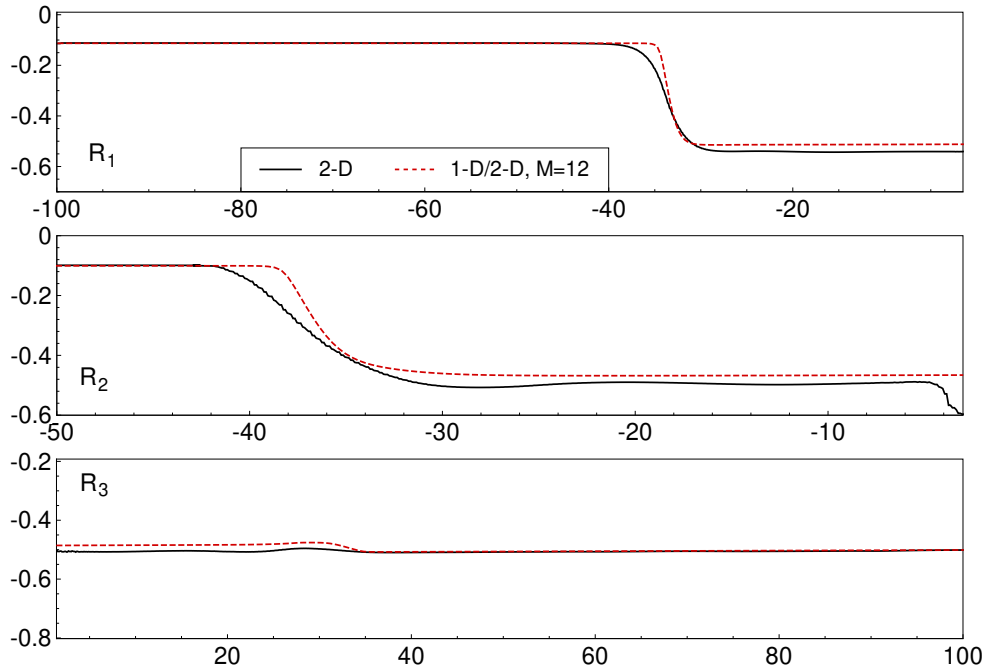

Figure 5.18: Example 6: Comparison of the flow discharge hu in reaches R_1, R_2 and R_3 computed at $t = 5023$ using the proposed 1-D/2-D coupling model with the averaged flow discharge from the 2-D computations.

⟨t6Fig4⟩

future, we plan to extend our 1-D/2-D coupling approach to more realistic situations, in which the cross-sectional area variation is taken into account in the 1-D shallow water system used to model the flow in each of the reaches.

Acknowledgments. The work of A. Chertock was supported in part by NSF grants DMS-1521051 and DMS-1818684. The work of A. Kurganov was supported in part by NSFC grant 11771201 and NSF grants DMS-1521009 and DMS-1818666.

References

UNET2001 [1] R. L. Barkau, *UNET: One-dimensional unsteady flow through a full network of open channels. User's manual*, tech. rep., U.S. Army Corps of Engineers, Hydrologic Engineering Center, Davis CA, 2001. Version 4.0.

BMK [2] A. Beljadid, A. Mohammadian, and A. Kurganov, *Well-balanced positivity preserving cell-vertex central-upwind scheme for shallow water flows*, Comput. & Fluids, 136 (2016), pp. 193–206.

Toro17 [3] F. Bellamoli, L. O. Müller, and E. F. Toro, *A numerical method for junctions in networks of shallow-water channels*, Appl. Math. Comput., 337 (2018), pp. 190–213.

Zentgraf2006 [4] T. Bleninger, J. D. Fenton, and R. Zentgraf, *One-dimensional flow modelling and a case study of the River Rhine*, in River Flow 2006, Proc. Int. Conf. on Fluvial Hydraulics, 2006, pp. 1963–1972.

HEC-RAS [5] G. Brunner, *HEC-RAS: River analysis system, hydraulic reference manual*, tech. rep., U.S. Army Corps of Engineers, Hydrologic Engineering Center, Davis CA, 2010. Version 4.1.

BEKP [6] S. Bryson, Y. Epshteyn, A. Kurganov, and G. Petrova, *Well-balanced positivity preserving central-upwind scheme on triangular grids for the Saint-Venant system*, M2AN Math. Model. Numer. Anal., 45 (2011), pp. 423–446.

Cunge [7] J. A. Cunge, F. M. Holly, and A. Verwey, *Practical Aspects of Computational River Hydraulics*, Pitman, London, 1980.

SaintVenant [8] A. J. C. de Saint-Venant, *Thèorie du mouvement non-permanent des eaux, avec application aux crues des rivière at à l'introduction des marèes dans leur lit.*, C.R. Acad. Sci. Paris, 73 (1871), pp. 147–154, 237–240.

FNQV [9] L. Formaggia, F. Nobile, A. Quarteroni, and A. Veneziani, *Multiscale modelling of the circulatory system: a preliminary analysis*, Comput. Vis. Sci., 2 (1999), pp. 75–83.

Fread73 [10] D. L. Fread, *Technique for implicit dynamic routing in rivers with tributaries*, Water Resour. Res., 9 (1973), pp. 918–926.

GR2 [11] E. Godlewski and P.-A. Raviart, *Numerical approximation of hyperbolic systems of conservation laws*, vol. 118 of Applied Mathematical Sciences, Springer-Verlag, New York, 1996.

GKS [12] S. Gottlieb, D. Ketcheson, and C.-W. Shu, *Strong stability preserving Runge-Kutta and multistep time discretizations*, World Scientific Publishing Co. Pte. Ltd., Hackensack, NJ, 2011.

GST [13] S. Gottlieb, C.-W. Shu, and E. Tadmor, *Strong stability-preserving high-order time discretization methods*, SIAM Rev., 43 (2001), pp. 89–112.

MASCARET1 [14] N. Gouta and F. Maurel, *A finite volume solver for 1D shallow-water equations applied to an actual river*, Internat. J. Numer. Meth. Fluids, 38 (2002), pp. 1–19.

MASCARET2 [15] N. Goutal, J. M. Lacombe, F. Zaoui, and K. El-Kadi-Abderrezzak, *MASCARET: a 1-D open-source software for flow hydrodynamic and water quality in open channel networks*, in River flow, vol. 1, Taylor & Francis, London, 2012, pp. 1169–1174.

Kro [16] D. Kröner, *Numerical schemes for conservation laws*, Wiley-Teubner Series Advances in Numerical Mathematics, John Wiley & Sons Ltd., Chichester, 1997.

KLshw [17] A. Kurganov and D. Levy, *Central-upwind schemes for the Saint-Venant system*, M2AN Math. Model. Numer. Anal., 36 (2002), pp. 397–425.

Kurganov01 [18] A. Kurganov, S. Noelle, and G. Petrova, *Semidiscrete central-upwind schemes for hyperbolic conservation laws and Hamilton-Jacobi equations*, SIAM J. Sci. Comput., 23 (2001), pp. 707–740.

Kurganov07 [19] A. Kurganov and G. Petrova, *A second-order well-balanced positivity preserving central-upwind scheme for the Saint-Venant system*, Commun. Math. Sci., 5 (2007), pp. 133–160.

KPW [20] A. Kurganov, M. Prugger, and T. Wu, *Second-order fully discrete central-upwind scheme for two-dimensional hyperbolic systems of conservation laws*, SIAM J. Sci. Comput., 39 (2017), pp. A947–A965.

KQRW [21] A. Kurganov, Z. Qu, O. Rozanova, and T. Wu, *Adaptive moving mesh central-upwind schemes for hyperbolic system of PDEs. Applications to compressible Euler equations and granular hydrodynamics.* Preprint.

KQW [22] A. Kurganov, Z. Qu, and T. Wu, *Well-balanced positivity preserving adaptive moving mesh central-upwind schemes for the Saint-Venant systems of shallow water equations.* In preparation.

LeV02 [23] R. LeVeque, *Finite volume methods for hyperbolic problems*, Cambridge Texts in Applied Mathematics, Cambridge University Press, Cambridge, 2002.

Liu12 [24] F. Liu and B. R. Hodges, *Dynamic river network simulation at large scale*, in Proceedings of the 49th Annual Design Automation Conference, ACM, 2012, pp. 723–728.

Liu14 [25] ——, *Applying microprocessor analysis methods to river network modelling*, Environ. Modell. Softw., 52 (2014), pp. 234–252.

liu2018well [26] X. Liu, J. Albright, Y. Epshteyn, and A. Kurganov, *Well-balanced positivity preserving central-upwind scheme with a novel wet/dry reconstruction on triangular grids for the Saint-Venant system*, J. Comput. Phys., 374 (2018), pp. 213–236.

MPS [27] E. Miglio, S. Perotto, and F. Saleri, *Model coupling techniques for free-surface flow problems: Part I*, Nonlinear Anal., 63 (2005), pp. e1885–e1896.

MIKE11 [28] MIKE11, *A modelling system for rivers and channels, reference manual*, tech. rep., DHI: Hørsholm, Denmark, http://manuals.mikepoweredbydhi.help/2017/Water_Resources/Mike_11_ref.pdf, 2017.

nessyahu90 [29] H. Nessyahu and E. Tadmor, *Non-oscillatory central differencing for hyperbolic conservation laws*, J. Comput. Phys., 87 (1990), pp. 408–463.

Novak [30] P. Novak, V. Guinot, A. Jeffrey, and D. E. Reeve, *Hydraulic modelling–an Introduction*, Spon Prees, New York, USA, 2010.

QF04 [31] A. Quarteroni and L. Formaggia, *Mathematical modelling and numerical simulation of the cardiovascular system*, in Handbook of Numerical Analysis, vol. 12, Elsevier, 2004, pp. 3–127.

MASCARETdoc [32] R. Rohan, A. Masson, C. Arlet, A. Rebaï, C. Jost, and C. Chaléon, *Development of a modelling tool of the Seine River and its main tributaries*, in Advances in Hydroinformatics, Springer, 2018, pp. 659–673.

SMSK [33] H. Shirkhani, A. Mohammadian, O. Seidou, and A. Kurganov, *A well-balanced positivity-preserving central-upwind scheme for shallow water equations on unstructured quadrilateral grids*, Comput. & Fluids, 126 (2016), pp. 25–40.

Steinebach [34] G. Steinebach, S. Rademacher, P. Rentrop, and M. Schulz, *Mechanisms of coupling in river flow simulation systems*, J. Comput. Appl. Math., 168 (2004), pp. 459–470.

Stoker [35] J. J. Stoker, *Water waves: The mathematical theory with applications*, vol. 36, John Wiley & Sons, 2011.

Swe [36] P. K. Sweby, *High resolution schemes using flux limiters for hyperbolic conservation laws*, SIAM J. Numer. Anal., 21 (1984), pp. 995–1011.

vanleer79 [37] B. van Leer, *Towards the ultimate conservative difference scheme, V. A second-order sequel to Godunov's method*, J. Comput. Phys., 32 (1979), pp. 101–136.

CCHE1D [38] W. Wu and D. A. Vieira, *One-dimensional channel network model CCHE1D version 3.0: Technical manual*, Tech. Rep. NCCH-TR-2002-02, National Center for Computational Hydroscience and Engineering, 2002.

WASH123 [39] G. T. Yeh, G. B. Huang, F. Zhang, H. P. Cheng, and H. C. Lin, *WASH123D: A numerical model of flow, thermal transport, and salinity, sediment, and water quality transport in WAterSHed systems of 1-D stream-river network, 2-D overland regime, and*

3-D subsurface media, tech. rep., EPA. Dept. of Civil and Environmental Engineering, Univ. of Central Florida, Orlando, FL, 2006.

Zhang14 [40] M. Zhang, Y. Xu, Z. Hao, and Y. Qiao, *Integrating 1D and 2D hydrodynamic, sediment transport model for dam-break flow using finite volume method*, Sci. China Phys. Mech. Astron., 57 (2014), pp. 774–783.